

Published in final edited form as:

*Neuroimage*. 2012 August 1; 62(1): 314–330. doi:10.1016/j.neuroimage.2012.04.042.

## Mapping Magnetic Susceptibility Anisotropies of White Matter in vivo in the Human Brain at 7 Tesla

Xu Li<sup>1,2,\*</sup>, Deepti S Vikram<sup>1,2</sup>, Issel Anne L Lim<sup>1,3</sup>, Craig K Jones<sup>1,2</sup>, Jonathan A.D. Farrell<sup>1,2</sup>, and Peter C. M. van Zijl<sup>1,2,\*</sup>

<sup>1</sup> F.M. Kirby Research Center for Functional Brain Imaging, Kennedy Krieger Institute, Baltimore, MD

<sup>2</sup> Department of Radiology, The Johns Hopkins University School of Medicine, Baltimore, MD

<sup>3</sup> Department of Biomedical Engineering, The Johns Hopkins University School of Medicine, Baltimore, MD

### Abstract

High-resolution magnetic resonance phase- or frequency- shift images acquired at high field show contrast related to magnetic susceptibility differences between tissues. Such contrast varies with the orientation of the organ in the field, but the development of quantitative susceptibility mapping (QSM) has made it possible to reproducibly image the intrinsic tissue susceptibility contrast. However, recent studies indicate that magnetic susceptibility is anisotropic in brain white matter and, as such, needs to be described by a symmetric second-rank tensor ( $\overline{\chi}$ ). To fully determine the elements of this tensor, it would be necessary to acquire frequency data at six or more orientations. Assuming cylindrical symmetry of the susceptibility tensor in myelinated white matter fibers, we propose a simplified method to reconstruct the susceptibility tensor in terms of a mean magnetic susceptibility,  $MMS = (\chi_{\parallel} + 2\chi_{\perp})/3$  and a magnetic susceptibility anisotropy,  $MSA = \chi_{\parallel} - \chi_{\perp}$ , where  $\chi_{\parallel}$  and  $\chi_{\perp}$  are susceptibility parallel and perpendicular to the white matter fiber direction, respectively. Computer simulations show that with a practical head rotation angle of around 20°–30°, four head orientations suffice to reproducibly reconstruct the tensor with good accuracy. We tested this approach on whole brain  $1 \times 1 \times 1 \text{ mm}^3$  frequency data acquired from five healthy subjects at 7 T. The frequency information from phase images collected at four head orientations was combined with the fiber direction information extracted from diffusion tensor imaging (DTI) to map the white matter susceptibility tensor. The MMS and MSA were quantified for regions in several large white matter fiber structures, including the corona radiata, posterior thalamic radiation and corpus callosum. MMS ranged from  $-0.037$  to  $-0.053$  ppm (referenced to CSF being about zero). MSA values could be quantified without the need for a reference and ranged between 0.004 and 0.029 ppm, in line with the expectation that the susceptibility perpendicular to the fiber is more diamagnetic than the one parallel to it.

© 2012 Elsevier Inc. All rights reserved

\*Correspondence: Xu Li, PhD, or Peter C.M. van Zijl, PhD F. M. Kirby Research Center for Functional Brain Imaging The Kennedy Krieger Institute 707 N. Broadway Street, Room G-25 Baltimore, MD, 21205 United States of America xuli@mri.jhu.edu or pvanzijl@mri.jhu.edu Tel: 443-923-9500 Fax: 410-614-1948.

**Publisher's Disclaimer:** This is a PDF file of an unedited manuscript that has been accepted for publication. As a service to our customers we are providing this early version of the manuscript. The manuscript will undergo copyediting, typesetting, and review of the resulting proof before it is published in its final citable form. Please note that during the production process errors may be discovered which could affect the content, and all legal disclaimers that apply to the journal pertain.

## Keywords

Magnetic susceptibility anisotropy; mean magnetic susceptibility; susceptibility tensor imaging; diffusion tensor imaging; white matter; high field

---

## Introduction

High-resolution magnetic resonance (MR) phase or frequency images acquired at high field show tissue contrast related to local magnetic susceptibility differences (Duyn et al., 2007). Many mechanisms can contribute to this susceptibility contrast (Albert et al., 1993; Schenck 2005), especially tissue concentration differences in non-heme iron, deoxyhemoglobin and myelin (Duyn et al., 2007; Haacke et al., 2005; Liu et al., 2011a; Fernandez-Seara et al., 2006; Hopkins and Wehrli 1997; Langham et al., 2009). In the brain, the concentrations of these compounds closely reflect physiological functioning, and, as such, could be potential biomarkers that may be noninvasively imaged using susceptibility contrast. Previously, MR phase data have been successfully used in susceptibility weighted imaging (SWI) to improve the visualization of veins because of the large phase shift caused by the high concentration of deoxyhemoglobin inside the vein (Haacke et al., 2004; Haacke et al., 2009; Mittal et al., 2009). Similarly, venous oxygenation can be determined using SWI (Fernandez-Seara et al., 2006; Langham et al., 2009). However, it is difficult to reproducibly quantify the information in phase/frequency shift images because the magnitude of the shift depends on the orientation of the organ with respect to the field due to the existence of a nonlocal relationship between the tissue susceptibility distribution and magnetic field perturbation that gives rise to the phase/frequency distribution (Li 2001; Marques and Bowtell 2005; Salomir et al., 2003). This has motivated the development of a new technique called quantitative susceptibility mapping (QSM) (de Rochefort et al., 2008; Li et al., 2011a; Liu et al., 2009; Liu et al., 2011; Schweser et al., 2011; Shmueli et al., 2009; Wharton and Bowtell 2010; Wu et al., 2011), which involves solving an ill-posed inverse problem to yield quantitative susceptibility images from the measured MR phase data. By collecting MR phase data at multiple head orientations with respect to the main magnetic field or by applying prior knowledge in the inverse regularization, the QSM technique makes it possible to image the intrinsic tissue susceptibility contrast with good image quality.

In addition to the measured MR phase depending on different head orientations relative to the main magnetic field, it was reported recently that the MR phase is sensitive to the orientation of brain tissue structures, such as white matter fibers or cortical ribbons, relative to the magnetic field (Denk et al., 2011; Lee et al., 2010). Such an orientation-dependent phase may be described by a generalized nonspherical Lorentzian model (Denk et al., 2011; He and Yablonskiy 2009) or, more commonly, using a second-rank symmetric magnetic susceptibility tensor,  $\overline{\chi}$  (Lee et al., 2010; Liu 2010). Similar to diffusion tensor imaging (DTI), where gradient orientations are used, determination of the six elements of such a tensor would require phase measurements for at least six independent spatial orientations of the organ with respect to the field, which is a bit impractical for clinical studies. In molecular studies, induced orientational anisotropy in liquid crystals (Emsley and Lindon 1975) or liquid solutions (Bastiaan et al., 1987; van Zijl et al., 1984) has been used to determine susceptibility tensor elements from anisotropic magnetic resonance parameters such as dipolar and quadrupolar couplings. Unfortunately, this is currently not yet possible for the macroscopic susceptibility anisotropies *in vivo*, where only macroscopic voxel information is available and where it is necessary to deconvolve the dipolar effects of neighboring tissues. Using an apparent susceptibility tensor model and MR phase data collected at a large number of head orientations (15-19), Li et al. demonstrated *ex vivo* in mouse brain and *in vivo* in human brain for a volunteer at 3 T that for most big white matter

fiber bundles the tensor map obtained by susceptibility tensor imaging (STI) agrees with the tensor map obtained by diffusion tensor imaging (DTI) (Li et al., 2011b; Liu 2010; Liu et al., 2011b; Mori et al., 1999). However, it remains quite challenging to perform *in vivo* susceptibility tensor imaging on human subjects due to the large number of independent head orientations required and the limited range of head rotation that a normal subject can perform inside an MRI head coil. On the other hand, the similarity found between the susceptibility tensor maps and diffusion tensor maps in the brain suggests the possibility of combining the fiber direction information extracted from DTI with the GRE phase measurements. In the present study, assuming cylindrical symmetry of the susceptibility tensor in white matter fibers (Wharton and Bowtell, 2011) defined by a parallel ( $\chi_{\parallel}$ ) and perpendicular ( $\chi_{\perp}$ ) magnetic susceptibility, we map the mean magnetic susceptibility ( $MMS = (\chi_{\parallel} + 2\chi_{\perp})/3$ ) and magnetic susceptibility anisotropy ( $MSA = \chi_{\parallel} - \chi_{\perp}$ ) of white matter tissues using the information from both GRE phase measurements and fiber directions estimated by DTI.

## Theory

### Magnetic susceptibility tensor and magnetic field shift

The tissue magnetic susceptibility is described by a second rank tensor,  $\overline{\overline{\chi}}$ . We will use standard tensor notation with the number of bars on top of a variable indicating rank; thus a second rank tensor has two bars, a first rank tensor (vector) one bar and a zero-rank tensor (scalar) no bars. Using the spherical Lorentz correction (Chu et al., 1990), the relative magnetic field shift distribution in space  $\delta B_z(\vec{r})$  (in units of ppm) measured in the MRI scanner can be derived (Appendix 1) to be (Liu 2010; Liu et al., 2011b):

$$\delta B_z(\vec{r}) = \frac{\Delta B_z(\vec{r})}{\mu_0 H_0} = \text{FT}^{-1} \left\{ \frac{1}{3} \widehat{H}_0 \cdot \text{FT} \{ \overline{\overline{\chi}}(\vec{r}) \} \cdot \widehat{H}_0 - \widehat{H}_0 \cdot \vec{k} \frac{\text{FT} \{ \overline{\overline{\chi}}(\vec{r}) \} \cdot \widehat{H}_0}{k^2} \right\} \quad (1)$$

where  $\mu_0$  is the vacuum permeability,  $\widehat{H}_0$  is the applied main magnetic field strength vector with magnitude  $H_0$  and unit vector  $\widehat{H}_0$ . FT and  $\text{FT}^{-1}$  denote the Fourier transform and its inverse, respectively;  $\vec{k}$  is the spatial frequency vector. The dot notation between tensors indicates a contraction producing a tensor with rank equal to the sum of the individual ranks of the original tensors minus two. Similar to the diffusion tensor, we can assume the susceptibility tensor is real and symmetric in tissue, i.e. there are only six independent tensor elements. Because the values of the tensor components depend on the selected spatial frame of reference, it is important to choose a proper frame to be able to compare results between laboratories. Three commonly used frames of reference are the laboratory frame, the subject frame, and the fiber diagonal frame (Figs. 1a–c). The lab frame is generally defined based on the direction of the main magnetic field flux density  $\overline{B}_0$ . However, the susceptibility tensor components will change if the head changes position with respect to  $\overline{B}_0$  and it is important to define an appropriate subject frame that can be compared between individuals. We define the subject frame ( $x'$ ,  $y'$ ,  $z'$ ) based on the commonly used anterior commissure – posterior commissure (AC-PC) line, defined as  $y'$ , and the midsagittal plane defined as ( $y'$ ,  $z'$ ). In the white matter, similar to DTI (Basser et al., 1994), the fiber diagonal frame of reference is defined by a principal axis aligned with the direction of the white matter axon fibers in that voxel ( $x''$ ). Notice that, since we will combine the diagonalized information from DTI with our STI determination, the main component will be in position 1 in the tensor, due to the convention in DTI to shift that component to that position. In the case of STI, this corresponds to the most paramagnetic (i.e. least negative) susceptibility component, along the  $x''$  axis.

In most of the QSM literature, the tissue susceptibilities are assumed isotropic, i.e. with  $\overline{\overline{\chi}} = \overline{\overline{\chi}} \overline{\overline{I}}$ , where  $\overline{\overline{I}}$  is the identity tensor. In the lab frame ( $\widehat{H}_0^{lab} = [0, 0, 1]^T$  and  $\overline{\overline{k}}^{lab} = [k_x, k_y, k_z]^T$ ), Eq. (1) can then be simplified to the well-known convolution relationship between the relative magnetic field shift  $\delta B_z(\vec{r})$ , and the susceptibility distribution determining it (Marques and Bowtell 2005; Salomir et al., 2003):

$$\delta B_z^{lab}(\vec{r}) = \text{FT}^{-1} \left\{ \left( \frac{1}{3} - \frac{k_z^2}{\|\overline{\overline{k}}^{lab}\|^2} \right) \text{FT} \{ \chi(\vec{r}) \} \right\} \quad (2)$$

However, the relative field shift distribution in the brain changes with the position of the subject's head in the main magnetic field. This orientation dependence has been utilized to stabilize the ill-posed QSM inverse problem by combining field shift data at different head orientations (Liu et al., 2009; Wharton and Bowtell 2010). In order to perform susceptibility tensor imaging (STI), i.e. map the susceptibility tensor elements in brain tissues, one needs to also combine the field shifts in the brain measured at different head orientations (Liu 2010; Liu et al., 2011b). When operating in the MRI laboratory frame of reference ( $x, y, z$ ), this is theoretically complicated, because we need to define different susceptibility tensor

fields for each orientation, i.e.  $\left(\overline{\overline{\chi}}^{lab}\right)_1, \left(\overline{\overline{\chi}}^{lab}\right)_2 \dots \left(\overline{\overline{\chi}}^{lab}\right)_N$  and the corresponding relative magnetic field shifts  $\left(\delta B_z^{lab}\right)_1, \left(\delta B_z^{lab}\right)_2 \dots \left(\delta B_z^{lab}\right)_N$ , where  $N$  is the total number of head orientations at which the relative magnetic field shifts are measured. For  $i=1 \dots N$ , Eq. (1) can then be written as:

$$\begin{aligned} \left(\delta B_z^{lab}\right)_i = & \text{FT}^{-1} \left\{ \left( \frac{1}{3} - \frac{k_z^2}{\|\overline{\overline{k}}^{lab}\|^2} \right) \text{FT} \{ \left(\chi_{33}^{lab}\right)_i \} \right. \\ & \left. - \frac{k_x k_z}{\|\overline{\overline{k}}^{lab}\|^2} \text{FT} \{ \left(\chi_{13}^{lab}\right)_i \} - \frac{k_y k_z}{\|\overline{\overline{k}}^{lab}\|^2} \text{FT} \{ \left(\chi_{23}^{lab}\right)_i \} \right\} \end{aligned} \quad (3)$$

Note that, for simplicity, we dropped the spatial position vector  $\vec{r}$  in Eq. (3), but that the magnetic susceptibility tensor components and the field shift are spatial functions of  $\vec{r}$ . For each head orientation, Eq. (3) is an underdetermined problem, i.e. with three unknown susceptibility tensor elements and only one experimental measurement per voxel. Additionally, in the lab frame of reference, it is not straightforward to combine experimental data collected at different head orientations, because the lab frame susceptibility tensor

fields also change with each orientation, i.e.  $\left(\overline{\overline{\chi}}^{lab}\right)_i \neq \left(\overline{\overline{\chi}}^{lab}\right)_j$  for  $i \neq j$ . In the subject frame of reference ( $x', y', z'$ ), on the other hand, the coordinate systems in both image space and k-space are affixed to the subject and we have a single well-defined susceptibility tensor field  $\overline{\overline{\chi}}^{sub}(\vec{r})$ . In this case, the direction of the main magnetic field changes with head orientation, i.e. we have  $\left(\widehat{H}_0^{sub}\right)_i$  for  $i=1 \dots N$ . Fortunately, the rotation matrix for this can be determined experimentally from the acquired images by coregistering them. Denoting the rotation matrix from the lab frame to the subject frame at the  $i$ th head orientation as  $\overline{\overline{R}}_i$ , we have  $\left(\widehat{H}_0^{sub}\right)_i = \overline{\overline{R}}_i \cdot \widehat{H}_0^{lab}$ . Similarly, for  $i=1 \dots N$ , we can write Eq. (1) in the subject frame as:

$$\begin{aligned} (\delta B_z^{sub})_i = & \text{FT}^{-1} \left\{ \frac{1}{3} (\widehat{H}_0^{sub})_i \cdot \text{FT} \left\{ \overline{\chi}^{sub} \right\} \cdot (\widehat{H}_0^{sub})_i \right. \\ & \left. - (\widehat{H}_0^{sub})_i \cdot \overline{k}^{sub} \frac{\overline{k}^{sub} \cdot \text{FT} \left\{ \overline{\chi}^{sub} \right\} \cdot (\widehat{H}_0^{sub})_i}{\|\overline{k}^{sub}\|^2} \right\} \end{aligned} \quad (4)$$

where  $\overline{k}^{sub} = [k_{x'}, k_{y'}, k_{z'}]^T$ . Note here that Eq. (4) is not well defined at the origin of the Fourier domain, i.e. when  $k_{x'} = k_{y'} = k_{z'} = 0$ . This may be better defined by estimating the derivatives (Li et al., 2011a), but because the origin of the Fourier domain only defines a constant offset, we will set the convolution kernel at this origin to zero for simplicity. Theoretically, with magnetic field shift measurements collected at  $N(N-6)$  different head orientations, it is then possible to solve for  $\overline{\chi}^{sub}$  from a system of linear equations composed of  $N$  equations in the form of Eq. (4) with  $i=1 \dots N$  (Liu 2010).

### Mapping the anisotropy of a cylindrically symmetric susceptibility tensor

When mapping the magnetic susceptibility anisotropy of human brain tissues *in vivo*, the rotation range is restricted and MR phase images can only be obtained at a small number of head orientations. We therefore simplify the susceptibility tensor model in two aspects. First, we assume that the susceptibility tensor in white matter fiber bundles is cylindrically symmetric along the main axonal axis (Fig. 1c), i.e. two of the three susceptibility eigenvalues are equal in its diagonal frame of reference ( $x''$ ,  $y''$ ,  $z''$ ). The susceptibility tensors in the subject and diagonal frames of reference are then related through the following tensor eigenvalue decomposition:

$$\overline{\chi}^{sub} = \overline{V} \cdot \overline{\chi}^{diag} \cdot \overline{V}^T = \sum_{i=1}^3 \chi_{ii}^{diag} \overline{v}_i^{sub} (\overline{v}_i^{sub})^T \quad (5)$$

in which  $\overline{\chi}^{diag} = \begin{bmatrix} \chi_{11}^{diag} & 0 & 0 \\ 0 & \chi_{22}^{diag} & 0 \\ 0 & 0 & \chi_{33}^{diag} \end{bmatrix}$  as in Fig. 1i,  $\overline{V} = [\overline{v}_1^{sub} \quad \overline{v}_2^{sub} \quad \overline{v}_3^{sub}]$  and  $\overline{v}_i^{sub}$  is the  $i$ th column eigenvector of the susceptibility tensor in the subject frame. Choosing  $\overline{v}_1^{sub}$  as parallel to the white matter fiber direction, the cylindrical symmetry of the susceptibility tensor therefore can be described by  $\chi_{22}^{diag} = \chi_{33}^{diag} = \chi_{\perp}$  and  $\chi_{11}^{diag} = \chi_{\parallel}$ . We can further define the mean magnetic susceptibility (MMS) and magnetic susceptibility anisotropy (MSA) as:

$$\text{MMS} = \chi_{avg} = (\chi_{\parallel} + 2\chi_{\perp}) / 3 \quad (6)$$

$$\text{MSA} = \chi_{ani} = \chi_{\parallel} - \chi_{\perp} \quad (7)$$

In the current study, where we intend to estimate the susceptibility tensor in white matter, we make a second assumption in that the diagonal frame of the susceptibility tensor of a white matter fiber coincides with that of the diffusion tensor for that fiber. Therefore, with the fiber direction information extracted from DTI when performing the tensor

diagonalization in the subject frame,  $\overline{v}_i^{sub}$  is known. Using the identity  $\sum_{i=1}^3 \overline{v}_i^{sub} (\overline{v}_i^{sub})^T = \overline{I}$ , we can then combine Eqs. (4) to (7) to derive:

$$(\delta B_z^{sub})_i = \text{FT}^{-1} \left\{ \frac{1}{3} (\widehat{H}_0^{sub})_i \cdot \text{FT} \left\{ \chi_{avg} \bar{T} - \frac{1}{3} \chi_{ani} \bar{T} \right\} \cdot (\widehat{H}_0^{sub})_i \right. \\ \left. - (\widehat{H}_0^{sub})_i \cdot \bar{k}^{sub} \frac{\text{FT} \left\{ \chi_{avg} \bar{T} - \frac{1}{3} \chi_{ani} \bar{T} \right\} \cdot (\widehat{H}_0^{sub})_i}{\|\bar{k}^{sub}\|^2} \right\} \quad (8)$$

in which  $\bar{T} = \bar{T} - 3\bar{v}_1^{sub}(\bar{v}_1^{sub})^T$ . In a similar way, one can derive the relationship between the relative magnetic field shift and  $\chi_{\parallel}$  and  $\chi_{\perp}$  as:

$$(\delta B_z^{sub})_i = \text{FT}^{-1} \left\{ \frac{1}{3} (\widehat{H}_0^{sub})_i \cdot \text{FT} \left\{ \chi_{\parallel} \bar{T}_1 + \chi_{\perp} (\bar{T} - \bar{T}_1) \right\} \cdot (\widehat{H}_0^{sub})_i \right. \\ \left. - (\widehat{H}_0^{sub})_i \cdot \bar{k}^{sub} \frac{\text{FT} \left\{ \chi_{\parallel} \bar{T}_1 + \chi_{\perp} (\bar{T} - \bar{T}_1) \right\} \cdot (\widehat{H}_0^{sub})_i}{\|\bar{k}^{sub}\|^2} \right\} \quad (9)$$

where  $\bar{T}_1 = \bar{v}_1^{sub}(\bar{v}_1^{sub})^T$ . In this study, we will mainly use Eq. (8) for solving MMS and MSA directly, but Eq. (9) can also be used for solving  $\chi_{\parallel}$  and  $\chi_{\perp}$ , which can subsequently be used to calculate MMS and MSA using Eqs. (6) and (7). Note here that the field shift in Eq. (8) is still defined in the subject frame of reference, but that the MMS and MSA are defined by the susceptibility eigenvalues in the fiber frame of reference and therefore orientation independent. Similar to the STI approach of (Liu 2010), we can construct a system of linear equations by stacking  $N(N-2)$  sets of equations and solve the inverse problem to obtain the MMS and MSA maps. As Eq. (8) has only two unknowns for each voxel, i.e. MMS and MSA, it may be solved with magnetic field shift measurements collected at much less head orientations than standard STI. However, it is not straightforward to do this with only two orientations. In order to understand this, first note that the equivalent coefficient of

$C = \frac{1}{3} - \frac{((\widehat{H}_0^{sub})_i \cdot \bar{k}^{sub})^2}{\|\bar{k}^{sub}\|^2}$  which is similar to the convolution kernel in the QSM problem with the susceptibility assumed isotropic (Liu et al., 2009; Wharton and Bowtell 2010). The coefficient function  $C$  is zero on a cone surface in the

Fourier domain, i.e. when  $\frac{((\widehat{H}_0^{sub})_i \cdot \bar{k}^{sub})^2}{\|\bar{k}^{sub}\|^2} = \frac{1}{3}$  and these zeros cannot be fully eliminated

unless we have at least three different head orientations, i.e. three different  $(\widehat{H}_0^{sub})_i$  (Liu et al., 2009). Therefore, in order to obtain a numerically stable solution of MMS and MSA without incorporating any other prior information for regularization, measurements of the field shift at three or more head orientations are required, while more measurements are expected to give better signal to noise ratio (SNR) and reconstruction accuracy. The final system of linear equations using  $N$  head orientations can be written as:

$$\begin{bmatrix} W_1 A_1 & W_1 & 0 & \cdots & 0 \\ W_2 A_2 & 0 & 0 & \cdots & 0 \\ \vdots & \vdots & \vdots & \ddots & \vdots \\ W_N A_N & 0 & 0 & \cdots & W_N \\ \alpha M_{out} & 0 & 0 & \cdots & 0 \end{bmatrix} \begin{bmatrix} \chi_{avg} \\ \chi_{ani} \\ \eta_1 \\ \eta_2 \\ \vdots \\ \eta_N \end{bmatrix} = \begin{bmatrix} W_1 (\delta B_z^{sub})_1 \\ W_2 (\delta B_z^{sub})_2 \\ \vdots \\ W_N (\delta B_z^{sub})_N \\ 0 \end{bmatrix} \quad (10)$$

where  $W_i$  is a selected weighting matrix for the  $i$ th head orientation and  $A_i$  represents the mapping relationship between  $\begin{bmatrix} \chi_{avg} \\ \chi_{ani} \end{bmatrix}$  and  $(\delta B_z^{sub})_i$  as shown in Eq. (8). The scalar unknown  $\eta_i$  is used to model possible global magnetic field shift offsets between measurements (Marques and Bowtell 2005; Schweser et al., 2011). The weighting matrix is supposed to indicate the data quality or SNR in the field shift measurement over space. In practice, we can use a brain-masked normalized GRE magnitude image as the weighting matrix (de Rochefort et al., 2010; Wharton and Bowtell 2010). In addition to the data fidelity terms, a simple regularization term is also added in Eq. (10) to improve numerical stability, with a 3D brain mask  $M_{out}$  and a regularization parameter  $\alpha$ . In Eq. (10), the brain mask  $M_{out}$  is multiplied on both  $\chi_{avg}$  and  $\chi_{ani}$ . The brain mask  $M_{out}$  is zero inside the brain area and is non-zero outside the brain. For high-resolution whole-brain mapping, Eq. (10) is an over-determined asymmetrical large linear system, which can be solved by iterative least square approaches such as the LSQR method (Paige and Saunders 1982).

Using MRI, the susceptibility-induced magnetic field shift can only be measured inside tissue containing water and not in air, for which the susceptibility is well known. Thus, similar to QSM, it is difficult to obtain an absolute MMS, and a well-defined internal tissue reference is needed to reproducibly report MMS quantities. On the other hand, since the MSA is calculated as the difference between two susceptibility tensor eigenvalues, the calculated MSA values are absolute values.

## Material and Methods

### Numerical simulations

A 3D 128×128×128 numerical head phantom (Fig. 2a) was designed to validate the proposed method and test the imaging performance under different conditions. The background area around the phantom had zero susceptibility, while the inside contained three ellipsoid regions (A – C) with cylindrically symmetric anisotropic susceptibility and one ellipsoid region (D) with isotropic susceptibility of 0.1 ppm. The rest of the head phantom had isotropic susceptibility of 0.05 ppm. Regions A, B and C had equivalent MMS of –0.1 ppm and MSA of 0.018 ppm. This MSA setting is close to the susceptibility anisotropy reported for white matter tissues in recent studies (Lee et al., 2010; Li et al., 2011b). As illustrated by the small arrows in Fig. 2a, the directions of the principal eigenvectors of the susceptibility tensors in regions A, B and C with respect to the subject frame of reference are parallel to  $x'$ ,  $y'$  and  $z'$ , respectively. In Figs. 2b and 2c, the central axial slices ( $z' = 64$ ) for the target MMS and MSA images are shown, respectively. At the normal head position, the subject frame was chosen to coincide with the lab frame. Magnetic field shift maps at five different head orientations, i.e. the normal head position, rotation about the  $y$ (AP) axis by  $\pm\theta$ , rotation about the  $x$  (RL) axis by  $\pm\theta$ , were simulated using Eq. (8). The head rotation angle  $\theta$  was set to 10°, 20°, 30°, 45°, 60° or 90°. The field shift map generated from an isotropic susceptibility head phantom with the same susceptibility distributions as the MMS of the anisotropic head phantom at the normal head position was also simulated using Eq. (2).

For the inverse calculation, a binary mask with ones inside the head region and zeros in the background was used for the weighting matrix as in Eq. (10). The regularization parameter  $\alpha$  was set to 20 to make the reconstructed MMS values outside the brain region to be close to zero (in the range of  $\pm 10^{-5}$  ppm). The convergence tolerance for the developed LSQR solver was set to  $1 \times 10^{-5}$  to ensure that good numerical accuracy was obtained in the solution. Image reconstruction performance was tested both with and without Gaussian noise. In the noisy condition, the field shift data had a SNR of 30. In addition, imaging

results were compared under varying inverse conditions, i.e. with different head rotation angles and using different numbers of head orientations (2 to 5). For this comparison, the field shift data simulated at the normal head position was always used; then, for a certain head rotation angle  $\theta$ , the field shift data at other orientations were added in the following order: rotation about the  $y$  (AP) axis by  $+\theta$ , rotation about the  $x$  (RL) axis by  $+\theta$ , rotation about the  $y$  (AP) axis by  $-\theta$ , rotation about the  $x$  (RL) axis by  $-\theta$ . Relative reconstruction error was used to quantify the imaging performance in the whole phantom as

$$RE = \sqrt{\sum_{n=1}^P (\chi_{t,n} - \chi_{r,n})^2 / \sum_{n=1}^P (\chi_{t,n})^2} \quad (11)$$

Where  $\chi_{t,n}$  and  $\chi_{r,n}$  are the target and reconstructed susceptibility values at the  $n$ th voxel in the phantom, respectively.  $P$  is the total number of voxels inside the phantom. Furthermore, to simulate possible errors in the DTI measurements and the DTI diagonalization procedure, random angular noise was added to the eigenvectors used in solving the inverse problem for mapping MMS and MSA. Angular noise was generated by rotating the original eigenvector around a randomly selected axis by a random angle with zero mean Gaussian distribution and standard deviation of  $5^\circ$ ,  $10^\circ$ ,  $15^\circ$ ,  $20^\circ$  or  $25^\circ$ . Such testing at different DTI eigenvector noise levels was conducted using simulated field shift data with a SNR of 30 and a head rotation angle of  $30^\circ$  at four head orientations. Error images were calculated by taking the difference between the calculated maps and the target maps. For this testing, maps of MMS, MSA,  $\chi_{\parallel}$  and  $\chi_{\perp}$  obtained by fitting MMS and MSA using Eq. (8) were compared to those obtained by fitting  $\chi_{\parallel}$  and  $\chi_{\perp}$  using Eq. (9). In addition to the MMS images, isotropic susceptibility images were also calculated from the simulated field shift maps that have SNR of 30, with head rotation angle of  $30^\circ$  at four head orientations using the multiple-orientation QSM method (Liu et al., 2009; Wharton and Bowtell 2010). For this approach, a system of linear equations similar to Eqs. (8) and (10) was used, except that terms associated with  $\chi_{ani}$  in Eq. (8) were removed. The weighting matrices, brain mask, regularization parameter, LSQR solver, and convergence tolerance were all similar to those used for calculating MMS and MSA.

### Human brain in vivo data acquisition

For the *in vivo* study, images were acquired at 7 T (Philips Healthcare, Best, Netherlands) using a 32-channel Novamedical head coil. Five healthy male subjects (30 to 36 years old) were studied after IRB approval and written informed consent. A 3D multi-echo GRE sequence was used with 1 mm isotropic resolution,  $220 \times 220 \times 110$  mm<sup>3</sup> field of view (FOV) with axial slab orientation, matrix size of  $224 \times 224 \times 110$ , TR/TE1/ $\Delta$ TE=45/2/2 ms, 9–16 echoes, SENSE factor of  $2.5 \times 1 \times 2$ , flip angle of  $9^\circ$ , and scan duration of 5:15 min per acquisition. Fat suppression was also accomplished using a water-selective ProSet 121 pulse. In order to minimize possible field drift during the scan, such as due to heating of the magnet bore during fast gradient switching, the 3D GRE sequence was run after other fast gradient-intense sequences such as MPRAGE and especially DTI, so that the magnet bore was warmed up before the GRE scan, which we found to result in reduced field drifting during the GRE scan. Each subject was scanned with his head placed at four different head orientations, i.e. normal supine position, tilting head to subject's right shoulder, tilting head to subject's left shoulder and tilting head to subject's back. The rotation angle for each orientation varied from  $5^\circ$  to  $22^\circ$  from the main  $\bar{B}_0$  axis. During the scan planning, all axial GRE images were positioned parallel to the AC-PC axis and perpendicular to the mid-sagittal plane, and the magnet was quickly shimmed every time the head position was changed. Note that even though shimming will change the background gradients over the brain, this is not an issue as these gradients are removed individually for each head position

during the data preprocessing. An MPRAGE scan with 1 mm isotropic resolution was acquired for anatomical referencing.

Because echo planar images are more distorted at 7 T, we acquired the DTI images on the same five subjects at 3 T (Philips Medical Systems, Best, Netherlands) using a single-shot EPI sequence, with 2.2 mm isotropic resolution,  $212 \times 212 \times 143 \text{ mm}^3$  FOV, reconstruction matrix size after zerofilling of  $256 \times 256 \times 65$ , TR/TE=6800/67 ms, b-value=700 s/mm<sup>2</sup>, 32 diffusion encoding gradients and scan duration of 4:25 min per acquisition. Two DTI acquisitions were performed on each subject and averaged to increase SNR and accuracy in the diffusion tensor calculation. For image coregistration and the selection of different ROIs, T<sub>1</sub>-weighted MPRAGE images were also acquired at 3 T with 1.1 mm isotropic resolution.

### Human brain data preprocessing

The flow chart in Figure 3 shows the detailed steps to process each dataset. For each subject, the first-echo GRE magnitude images acquired at all head orientations were coregistered to the first-echo magnitude image acquired at the normal supine head position by rigid body linear transformation using the FSL FLIRT tool (Jenkinson et al., 2002; Smith et al., 2004). The coregistration transformation matrix was then applied to the real and imaginary data at every echo time (TE) to generate the coregistered real and imaginary images. These images were further converted to the coregistered magnitude and phase images. After coregistration, all data are in the subject frame of reference and the rotation matrix from the lab frame to the subject frame  $\overline{\overline{R}}$  as well as the main magnetic field direction in the subject frame  $(\widehat{H}_0^{sub})_i$  can then be calculated based on the scanner's angulation parameters and the coregistration transformation matrix. Phase wraps in the coregistered phase images were subsequently removed by a Laplacian-based phase unwrapping method (Li et al., 2011a). Next, for each imaging voxel, the frequency shift  $\Delta f$  was calculated by least squares fitting of the linear slope of the phase  $\varphi$  as function of TE using eight echoes. The frequency shift in Hz is proportional to the magnetic field shift as  $\Delta f = \gamma \Delta B_z / 2\pi$ , where  $\gamma$  is the gyromagnetic ratio in radians/Tesla. The relative magnetic field shift in ppm therefore can be calculated by dividing  $\Delta f$  with the spectrometer frequency (298 MHz in our case). The linear fitting of the phase over time also provides an estimate of the initial phase  $\varphi_0$ , which can be used to exclude some voxels that have unreliable phase measurement due to turbulent flow, partial volume effect or extremely high in-voxel resonance frequency shift (Schweser et al., 2011). Before we can map the MMS and MSA, another important preprocessing step is to remove the slowly-varying background gradient field which is mainly generated by the big susceptibility changes at the air-tissue interfaces. Several techniques have been developed for this purpose, including polynomial fitting (Duyn et al., 2007), dipole fitting (de Rochefort et al., 2010; Wharton and Bowtell 2010) and the sophisticated harmonic artifact reduction for phase data (SHARP) (Schweser et al., 2011; Wu et al., 2011). Here, we used the dipole fitting method to model the background gradient field for each head orientation. This was achieved by solving a minimization problem to determine the susceptibility sources outside of the brain mask that generate a background gradient field close to the measured one:

$$\min_{\chi} \left( \left\| W_i \left( \text{FT}^{-1} \left\{ \frac{1}{3} - \frac{((\widehat{H}_0^{sub})_i \cdot \overline{k}^{sub})^2}{\|\overline{k}^{sub}\|^2} \right\} \text{FT} \{ \chi \} \right) - (\delta B_z^{sub})_i \right\|_2^2 + \beta^2 \|M\chi\|_2^2 \right) \quad (12)$$

where  $W_i$  is a weighting matrix,  $M$  is a brain mask and  $\beta$  is a regularization parameter. In the present study, for each head orientation, we used the mean normalized GRE magnitude

image at the sixth echo (TE=12 ms) as the weighting matrix. The brain mask  $M$  was generated by using FSL BET tool (Smith 2002; Smith et al., 2004) on the magnitude image acquired at the normal supine head position. The mask was applied with a value of one inside the brain area and zero outside of the brain area. The regularization parameter  $\beta$  was set to be 1000. An iterative conjugate gradient based solver was developed for solving this minimization problem. The magnetic field shift distribution created by these fitted susceptibility sources was then subtracted from the original measured one and the residual magnetic field shift was used for susceptibility calculation.

The DTI images were coregistered to the sixth echo (TE=12 ms) GRE magnitude image acquired at the normal supine head position, which showed appropriate tissue contrast for comparison. Trilinear interpolation was used in the coregistration. The diffusion tensor calculation was conducted using DtiStudio (Jiang et al., 2006). The principal eigenvector (PEV) map was then used for the mapping of MMS and MSA. The DTI fractional anisotropy (FA) maps were also obtained for image comparison and segmenting the white matter fibers.

### Susceptibility calculation

For the human *in vivo* study, the inverse calculation of MMS and MSA was conducted as described in Eq. (10) using the relative magnetic field shift maps at four different head orientations and the eigenvector maps extracted from DTI measurements. The GRE magnitude images at the sixth echo (TE=12 ms) were used for the weighting matrices, the regularization parameter  $\alpha$  was set to 20. The convergence tolerance for the developed solver was selected to be  $3 \times 10^{-5}$  using the L-curve method (Hansen 2000). The brain mask  $M_{out}$  is set to be the complement of the brain mask  $M$  used in the dipole fitting method described in the previous section. For each subject, white matter throughout the whole brain was selected by segmenting a coregistered  $T_1$  weighted image using a simple seed region growing method. This whole-brain white matter was used for MMS and isotropic susceptibility referencing by shifting the calculated MMS values so that the mean MMS value of white matter was  $-0.03$  ppm. This value was chosen because it led to a negligible MMS for cerebral spinal fluid (CSF), which is a common reference region used in the field when assuming an isotropic susceptibility. However, unlike ventricles, large white matter regions are easy to select, and the MMS values inside these white matter regions have smaller spatial variations. We therefore used this indirect way to reference to MMS of CSF being 0 ppm. The corresponding susceptibility parallel and perpendicular to the fiber direction, i.e.  $\chi_{\parallel}$  and  $\chi_{\perp}$ , were also calculated using the fitted MMS and MSA as

$$\chi_{\parallel} = \chi_{avg} + \frac{2}{3}\chi_{ani} \text{ and } \chi_{\perp} = \chi_{avg} - \frac{1}{3}\chi_{ani}.$$

In order to illustrate the presence of susceptibility anisotropy in white matter fibers, an apparent susceptibility map was calculated from magnetic field shift map acquired at each single head orientation using the LSQR method described in (Li et al., 2011a). This method solves the minimization problem in image space to satisfy the data fidelity condition and does not use prior structure information for regularization, so there is minimum unwanted smoothing in the calculated susceptibility image (Wharton and Bowtell 2010). Note that the apparent susceptibility maps were calculated assuming isotropic susceptibility in all tissues. All the data preprocessing and susceptibility calculations were implemented using MATLAB R2011b (The Mathworks, Natick, MA).

### Region of interest selection

To obtain a quantitative evaluation of MMS in different brain tissues and MSA in several central white matter fiber bundles, we selected regions of interest based on a human brain

atlas (Oishi et al., 2009). The T<sub>1</sub>-weighted image was coregistered to the GRE magnitude images for each subject. The T<sub>1</sub>-weighted image in the “Type II Eve Atlas” was then coregistered to the T<sub>1</sub>-weighted image of each subject using both affine transformation and single-contrast Large Deformation Diffeomorphic Metric Mapping (LDDMM) (Beg et al., 2005). Both the affine and LDDMM coregistration were performed using freely available MRISTUDIO software (www.mristudio.org). The combined transfer matrix was then applied to a segmentation map that was defined in population-averaged DTI data, i.e. the white matter parcellation map (Mori et al., 2008) and a segmentation map based on the measured isotropic susceptibility image of the Eve subject calculated using the multiple-orientation QSM method. These two segmentation maps are both in the Eve atlas space and can be transferred to subject space by applying the coregistration transfer matrix. Based on the coregistered white matter parcellation map in the subject space, we selected several deep white matter regions including the posterior thalamic radiations (PTR, including optic radiations), corona radiata (CR, including anterior, superior and posterior sections) and corpus callosum (CC, including the genu, the body, and the splenium of corpus callosum). Due to visible inaccuracies in the MSA reconstruction map, white matter regions close to the deep nuclei were not assessed. Using the coregistered susceptibility segmentation map in subject space, several deep gray matter regions were also selected, including substantia nigra, red nucleus, globus pallidus, putamen and caudate nucleus. In addition, ventricular regions were selected for evaluating the MMS in CSF. In order to minimize partial volume effects, the selected white matter regions were multiplied by a DTI FA mask that was generated by thresholding the FA map at 0.25. The white matter and CSF ROIs selected in this way were further eroded by 1 mm and the selected deep gray matter ROIs were eroded by 2 mm.

## Results

### Numerical phantom results

In order to compare image appearance using anisotropic and isotropic approaches, we first performed forward calculations of the relative field shift map ( $\delta B_z^{sub}(\vec{r})$ ) using the susceptibility tensor model at the normal head position. The anisotropic result is shown in Fig. 2d, while the simulated field shift map generated from an isotropic susceptibility head phantom with the same susceptibility distribution as the MMS of the susceptibility tensor model is illustrated in Fig. 2e. Both field shift maps show strong dipole patterns around structure edges. However, as shown in Fig. 2f, differences are apparent inside the anisotropic structures and close to their edges. These differences are on the order of  $\pm 5 \times 10^{-3}$  ppm, which corresponds to resonance frequency shifts of  $\pm 1.5$  Hz at 7 T and  $\pm 0.64$  Hz at 3 T. The range of such kind of difference is mainly determined by the MSA of the susceptibility tensor in these anisotropic tissues, which was set to 0.018 ppm in the present phantom.

The performance of the image analyses under different inverse conditions using noise-free field shift data is illustrated in Fig. 4, in which the relative reconstruction errors in MMS (Fig. 4a) and MSA (Fig. 4b) are compared for a head rotation angle range from 10° to 90° and for two to five head orientations. It can be seen that the use of only two head orientations gives unacceptable errors. Example images of the reconstructed MMS and MSA using four head orientations with rotation angle of 30° are also shown in Figs. 4a, b. These images compare well to the target MMS and MSA maps in Figs. 2b and 2c, with relative reconstruction errors for MMS and MSA in the whole head phantom of 0.02% and 1.2%, respectively. Note that the relative reconstruction error for MSA will always be bigger than the one for MMS, because the MSA distribution has one order of magnitude smaller dynamic range. The estimated MMS and MSA for the three anisotropic regions (A–C) were

$-0.10 \pm 0.000016$  ppm and  $0.018 \pm 0.000060$  ppm (mean  $\pm$  standard deviation), respectively, while MSA for the isotropic regions was  $0.0000 \pm 0.000078$  ppm. The reconstructed MSA values under the other inverse conditions are illustrated in Figs. 4c, 4d and 4e for the anisotropic regions that have principal eigenvector parallel to  $z'$  (region C), perpendicular to  $z'$  (regions A and B) and isotropic regions, respectively, showing good agreement with the expectation for three head orientations at  $30^\circ$  and four orientations at  $20^\circ$ .

Simulations using noisy field shift maps (SNR = 30) are illustrated in Fig. 5. In Figs. 5a and 5b, the example MMS and MSA maps using 4 head orientations with rotation angle of  $30^\circ$  gave relative errors of 2.1% and 60.6%, respectively. The estimated MMS and MSA for all of the anisotropic regions were  $-0.10 \pm 0.00092$  ppm and  $0.015 \pm 0.0039$  ppm, respectively, while the estimated MSA for the isotropic regions was  $0.0019 \pm 0.0031$  ppm. The reconstructed MSA values under the other inverse conditions are illustrated in Figs. 5c, 5d and 5e for the anisotropic regions that have principal eigenvector parallel to  $z'$  (region C), perpendicular to  $z'$  (regions A and B), and isotropic regions, respectively, showing excellent agreement with expectation for three to four head orientations at 45 degrees and reasonable performance for three to four orientations at 30 degrees.

Figs. 6a–d illustrate the influence of increasing angular noise in the DTI eigenvectors on the imaging performance for field shift data with SNR of 30, head rotation angle of  $30^\circ$  and four head orientations. It can be seen that while the relative reconstruction errors for MMS and  $\chi_{\perp}$  are quite insensitive to angular noise, this is not the case for MSA and  $\chi_{\parallel}$ . In addition, negligible differences are observed between the imaging results obtained by fitting MMS and MSA using Eq. (8) and those obtained by fitting  $\chi_{\parallel}$  and  $\chi_{\perp}$  using Eq. (9). Example reconstructed MMS and MSA maps with a DTI eigenvector noise standard deviation of  $10^\circ$  are shown in Figs. 6e and 6h. The MMS compares well to the target image, but the MSA does not, which is reflected in the corresponding error images (Figs. 6f, i) and the relative reconstruction errors for the MMS and MSA distributions in the whole head phantom of 2.2% and 64.6%, respectively. The estimated MMS and MSA in the three anisotropic regions were  $-0.10 \pm 0.0018$  ppm and  $0.014 \pm 0.0062$  ppm, respectively. It was also observed that the reconstruction errors in the MSA (Fig. 6i) depended on the fiber directions in the anisotropic regions; For instance, compared to regions A and C, region B had a larger mean MSA error. Such variation is caused by the specific selection of head rotation axes and rotation angles. The reason is that certain rotations don't change the direction (and thus the field shift) of particular fibers with respect to the main magnetic field, leading to a worse inverse condition for estimating the susceptibility tensor in these fibers. For example, rotation about the  $y$  (AP) axis does not change the direction of fibers in the  $y$  direction relative to the main magnetic field.

The isotropic susceptibility image reconstructed using the multiple-orientation QSM method and the corresponding error image with respect to the target MMS map are shown in Figs. 6g and 6j, respectively. Clear deviations can be seen in and around the anisotropic structures.

### In vivo results

An example of an axial slice of the relative magnetic field shift map in the subject frame for a single subject is shown at four different head orientations in Figs. 7a–d. As expected, these magnetic field shift maps show strong dipole patterns around different tissue structures, and obvious orientation dependence is observed between these maps. The calculated apparent susceptibility maps for this slice at the same four head orientations are shown in Figs. 7e–h. These maps were obtained by solving the inverse problem for the field shift maps in Figs. 7a–d under the assumption of isotropic susceptibility and by using only a single orientation. In order to highlight the white matter, we used a reversed gray scale for both the field maps

and the apparent susceptibility maps, so that the negative values are bright. The apparent susceptibility images give a more quantitative representation of the tissue susceptibility than the field shift maps, as can be seen in the iron rich deep gray matters such as the globus pallidus, putamen and caudate nucleus, which are much better defined in the susceptibility images. However, in some white matter fibers such as the internal capsule (arrows in Fig. 7h) and the optic radiations (arrows in Fig. 7f), the apparent susceptibility images show noticeable asymmetry between left and right hemispheres due to a remaining orientation dependence in the susceptibility map. This agrees with previous reported findings at 3 T (Li et al., 2011a), but is more apparent at 7 T due to the better image quality (SNR) and the larger frequency contrast (proportional to the field) that is used to determine the same susceptibility difference in ppm. The remaining head orientation dependence in the apparent susceptibility images suggests that the magnetic susceptibility in white matter tissues is anisotropic and that fitting using the susceptibility tensor model is needed to better estimate the susceptibility properties of white matter tissues.

Using the approach outlined in the theory section, we subsequently fitted MMS, MSA,  $\chi_{\parallel}$  and  $\chi_{\perp}$  for the whole brain using the combination of GRE phase data and DTI-based fiber directions. Figure 8 shows axial views of MMS, MSA, DTI colormap,  $\chi_{\parallel}$  and  $\chi_{\perp}$  for a single subject at three different brain locations. In order to highlight white matter, we used a reversed gray scale for MMS,  $\chi_{\parallel}$  and  $\chi_{\perp}$  maps, but normal scale for MSA maps. In order to illustrate the quality of the MMS and MSA maps in the whole brain, a coronal, sagittal, and another axial view of the MMS, MSA, and DTI colormap of the same subject are shown in Fig. 9. It is clear from these figures that MMS maps provide good contrast between white matter and gray matter over the whole brain, while the MSA maps are relatively noisy, especially around tissue interfaces. When comparing images of  $\chi_{\parallel}$  (Figs. 8j–l) and  $\chi_{\perp}$  (Figs. 8m–o), it can be seen that the contrast between gray and white matter is generally reduced in  $\chi_{\parallel}$  maps indicating that the parallel component of the susceptibility tensor in white matter is more paramagnetic than the perpendicular component, in line with the positive anisotropy measured in the MSA images. This trend is visible in most of the brain, but some deviations can be seen around very paramagnetic gray matter nuclei (e.g. in the posterior limb of the internal capsule), which may indicate some remaining inaccuracy in the inverse fitting procedure (see discussion section).

In order to better compare the appearance of the fitted MSA with the diffusion fractional anisotropy (FA) derived from DTI, we applied a threshold of  $FA > 0.25$  to both MSA and FA maps from a selected subject (Figs. 9j–o). In general, the appearance of the MSA contrast is consistent with that of FA contrast in most white matter regions. However, the MSA maps are noisier and have a larger spatial variation in the white matter regions.

Finally, we selected several large central white matter fiber bundles to quantify the MMS and MSA values in these brain areas. In addition, MMS values for some deep nuclei were quantified for comparison. For gray matter regions or other areas with small FA values, the eigenvectors of the diffusion tensor obtained by DTI are not very reliable, which would be reflected in the fitted MSA. Therefore we only analyzed MSA in the large white matter fibers. The selected white matter regions are illustrated in Figs. 10a–d and the MMS and MSA averaged over five subjects are listed in Table 1 and illustrated in Figs. 10e and 10f, respectively. The corresponding calculated  $\chi_{\parallel}$  and  $\chi_{\perp}$  in selected ROIs averaged over the five subjects are also listed in Table 1. It can be seen from Fig. 10 that the MMS values for different white matter structures have small inter-subject variation compared to the deep nuclei. All of the selected white matter fiber bundles have a slightly positive mean MSA ranging from 0.005 – 0.03 ppm, with the MSA in the body of corpus callosum being the highest. In order to test whether there was a possible relationship between the accuracy of the MSA and the magnitude of the diffusion anisotropy in white matter fibers, a scatter plot

(Fig. 10g) was made of MSA versus FA for all selected white matter voxels in the five subjects. No obvious relationship was observed.

## Discussion

Mapping of the magnetic susceptibility properties of brain tissues has attracted a lot of interest in recent years because of its impressive contrast between different brain structures and its sensitivity to several biologically relevant compounds such as iron and myelin. Quantitative mapping of tissue susceptibility (QSM) opens up the possibility of potential application to the diagnosis and monitoring of several important neurodegenerative diseases such as Alzheimer's disease, Huntington's disease, Parkinson's disease and multiple sclerosis (Zecca et al., 2004). Originally, most QSM studies assumed tissue susceptibilities to be isotropic, but recent experimental evidence (Lee et al., 2010; Li et al., 2011b; Liu et al., 2011b) indicates that the magnetic susceptibility in white matter fibers is anisotropic and has to be described by a tensor (Liu 2010). Mapping of this anisotropy would require acquisition of field maps for at least six brain orientations in the magnetic field, which would be prohibitive in practice for most organs *in vivo*. In addition, the anisotropic effects are small (on the order of 0.01 – 0.02 ppm (Lee et al., 2010; Li et al., 2011b)), and the determination of susceptibilities is already complicated due to the requirement of solving an inverse problem (de Rochefort et al., 2010; Li 2001; Wharton and Bowtell 2010). As a first simplification towards determining anisotropies with a reduced number of orientations, we used the assumption of a cylindrically symmetric tensor for parallel fiber bundles. This allowed us to derive practical expressions (Eqs. 8, 9) for field shifts in terms of several anisotropy parameters, namely mean magnetic susceptibility (MMS) and magnetic susceptibility anisotropy (MSA), or the magnetic susceptibility parallel and perpendicular to the fiber, respectively. Defined in a subject-based frame of reference, the unknowns in these equations are the susceptibility parameters and the orientation of the fiber structures with respect to the midsagittal plane and the AC-PC line. Knowledge of the fiber orientations, e.g. from DTI, then allows determination of these parameters with fewer head orientations. We subsequently performed simulations with a numerical head phantom to determine the number of head orientations and the range of head angles needed to have reasonable noise characteristics for solving the inverse tensor problem, and then applied this approach to five human volunteers to measure MMS, MSA,  $\chi_{\parallel}$  and  $\chi_{\perp}$  in white matter.

## Simulations

Two major factors that affect the inverse condition for mapping MMS and MSA using the proposed method are head rotation angle and the number of head orientations. In general, the use of more head orientations, i.e. more measurement data, would improve the inverse condition at the expense of longer scan time and reduced subject comfort. The head rotation angles will have an optimum setting depending on the number of head orientations used. However, the angle range is restrained in practice by the RF coil and physical limitations of the subject. Our simulations using a rotation angle range of 10° to 90° and 2 to 5 head orientations (Figs. 4, 5) show that the best inverse condition is obtained for 5 head orientations with 40–60° rotation angles. At first this may seem a bit odd in that one may expect 90° to provide a more accurate estimate of MSA. However, while a rotation angle of 90° gives the best imaging performance when only two head orientations are used (Fig. 4, 5), it has to be realized that this angle does not necessarily give the best inverse condition for mapping MMS and MSA for more head orientations. From Eq. (4) or Eq. (8), we can see that the relative magnetic field shift in k space, i.e.  $\text{FT} \left\{ \left( \delta B_z^{sub} \right)_i \right\}$ , measured at the  $i$ th head orientation can be considered as the sum of two different projections of the susceptibility tensor in k space, i.e.  $\text{FT} \left\{ \overline{\chi}^{sub} \right\}$ , on the direction of  $\left( \widehat{H}_0^{sub} \right)_i$ . Therefore, when using all the

field measurements collected at different head orientations for estimating the susceptibility tensor, the best inverse condition is achieved when all projections are least dependent on each other. This optimum condition is not straightforward to be derived in theory and generally needs to be tested using computer simulations. In practice, a general strategy to achieve a good inverse condition for STI would be to make the  $N$  head orientations uniformly distributed across a spherical surface (Liu et al., 2011b). Secondly, using the head rotation protocol in the present study, a rotation angle of  $90^\circ$  actually makes some field shift measurements interdependent. For example, the field shift collected for a  $90^\circ$  head rotation about the  $y$  (AP) axis (with  $(\widehat{H}_0^{sub})_i = [1, 0, 0]^T$ ) depends linearly on the shift with  $-90^\circ$  rotation about the  $y$  (AP) axis (with  $(\widehat{H}_0^{sub})_i = [-1, 0, 0]^T$ ).

Large reconstruction errors were found when limiting the mapping of MMS and MSA to two head orientations. This is not unexpected because of the ill-posed inverse condition for this situation, as mentioned in the theory. Previous QSM and STI studies at 3 T (Li et al., 2011b; Schweser et al., 2011) reported head rotation angles as large as  $40^\circ$ – $50^\circ$ . However, our experience was that  $20^\circ$ – $30^\circ$  was the maximum rotation angle our human subjects could comfortably reach in our smaller 32-channel head coil at 7 T. Based on our simulation results with noise free data (Fig. 4), a rotation angle of  $20^\circ$ – $30^\circ$  with four head orientations has significantly better performance than three head orientations and comparable performance to five orientations. Therefore, we chose four head orientations for mapping MMS and MSA *in vivo*.

For simplicity, the simulation protocol was designed in a way that each head orientation was produced by rotating the head phantom about one single axis with respect to baseline, even though different head orientations may have different rotation axes ( $y$  (AP) axis or  $x$  (RL) axis). Previous QSM studies suggest that rotation about more than one axis for each head orientation may further improve the inverse conditioning (Wharton et al., 2010). This may ultimately make the use of three head orientations sufficient to reconstruct the susceptibility tensor components with enough accuracy, but the use of more head orientations would always improve the imaging accuracy and the reconstructed image quality.

As shown in our simulations in Figs. 5a, and 6a, e, h, the use of four head orientations with  $30^\circ$  rotation angle at  $\text{SNR}=30$ , provides reconstructed MMS maps that compare well to the target MMS. The reconstructed MSA maps look much noisier and compared to the target MSA (Fig. 2c), the fitted MSA values in anisotropic regions that have a principal eigenvector perpendicular to  $z'$  are slightly underestimated (Fig. 5d), while they are overestimated in anisotropic regions with principal eigenvector parallel to  $z'$  (Fig. 5c) and in isotropic regions (Fig. 5e). Therefore, care has to be taken when interpreting the results of average analysis over all anisotropic regions. For instance, in the present head phantom, the volume with tensor principal eigenvector perpendicular to  $z'$  (A and B) is much larger than that with tensor principal eigenvector parallel to it (C) and the average MSA value over all the anisotropic regions consequently shows an underestimation.

Figs. 6a–d show that the determination of MMS, MSA,  $\chi_{\parallel}$  and  $\chi_{\perp}$  using Eqns. 8 and 9 is quite comparable. Interestingly, Eqn. 9 provides more accurate estimates if the fiber angles are well known, but it is also more sensitive to errors in these angles.

Finally, it is clear from the results in Fig. 6j that measurement of bulk susceptibilities will also be affected by the presence of tissue structures with an anisotropic magnetic susceptibility. While the reconstructed isotropic susceptibility image obtained using the multiple-orientation QSM method (Fig. 6g) looks similar, the difference image (Fig. 6j) between this and the target MMS map shows clear deviations inside the anisotropic regions

and around the edges of these structures, again with fibers parallel to  $z'$  showing an overestimation and perpendicular to  $z'$  an underestimation. Thus, with a practical constrained head rotation range in humans of about  $20^\circ$ – $30^\circ$ , the isotropic susceptibility distribution fitted with non-tensor-based QSM would most likely deviate from the real tissue MMS in and around anisotropic structures.

### In vivo human MMS and MSA

Using four brain positions and the fiber orientations (eigenvectors) in the subject frame determined from DTI, we were able to measure reproducible MMS and MSA values for several large white matter fibers (Fig. 10 and Table 1). Notice that while the MMS numbers are relative and need to be compared to a standard, the MSA values are absolute as they are based on a difference between two susceptibilities. For the MMS we first tried to reference to CSF (assigned value of 0.00 ppm) in the ventricles, but CSF showed a large range of possible values, probably due to partial volume effects with neighboring structures and proximity to deep gray matter structures. On the other hand, white matter structures occupy a large fraction of the brain and show a reproducible relatively compact range of possible MMS values. We found a reproducible approach for referencing in assuming an average MMS of  $-0.03$  ppm for white matter, which corresponds to a measured negligible MMS in the ventricles (Fig. 10e). The MMS values for white and gray matter structures referenced this way show excellent reproducibility between subjects (Fig. 10).

The MSA values show that the white matter anisotropy is on the order of  $0.01$  –  $0.03$  ppm, with most structures in the  $0.01$  ppm range. This compares favorably with previous postmortem studies on corpus callosum fibers, which showed a susceptibility difference of  $0.006$  to  $0.012$  ppm between white matter fibers parallel and perpendicular to the magnetic field (Lee et al., 2010). In addition, a recent biophysical model assuming that the susceptibility anisotropy in white matter originates predominantly from the organized anisotropic lipid molecules in myelin predicted a  $0.018$  ppm susceptibility difference between fibers parallel and perpendicular to the field (Li et al., 2011b). A difference of comparable magnitude ( $0.026$  ppm) was measured *ex vivo* in mouse brain in the hippocampal commissure (Li et al., 2011b). Also, using STI for *in vivo* human brain, a susceptibility anisotropy of  $0.022$  ppm was measured in superior white matter when using a definition similar to the MSA (Li et al., 2011b). The differences between the current study and these reported literature values can be considered small in view of tissue heterogeneity, the difference in resolution between the DTI and GRE data used to derive these values, the poor inverse conditioning because of restricted subject head movement, and the inescapable effects of coregistration errors.

Recent STI studies in both *ex vivo* mouse brain and *in vivo* human brain have demonstrated the possibility of using susceptibility anisotropy information to study the white matter fiber orientations (Li et al., 2011b; Liu et al., 2011b) in a manner similar to DTI. When evaluating this possibility it is interesting to realize that even though both STI and DTI use information based on organized white matter microstructures, the origin of the measured signals is due to very different physical mechanisms and has a totally different MRI acquisition strategy. This difference is somewhat reflected in the interesting result in Fig. 10g that no obvious relationship is observed between MSA and DTI FA. This is not unexpected, because the susceptibility anisotropy is most likely based on myelin anisotropy (Lee et al., 2010; Li et al., 2011b), while the diffusion anisotropy is mainly determined by water motion restricted by axonal symmetry plus a 20–30% myelin contribution (Beaulieu 2002). In order to perform the MMS and MSA determinations in the present study, we assumed that the susceptibility tensor in white matter fibers has the same principal axis as the diffusion tensor. This approach greatly reduced the number of unknowns in the STI fitting process and made it more feasible to map the susceptibility anisotropy in human white matter *in vivo*.

Despite the difference in resolution between our DTI and GRE data, a reasonably reproducible measurement of MMS and MSA was possible using multi-echo GRE phase measurements acquired at four different head orientations. Based on the small size of the anisotropy, however, it currently does not seem straightforward to simultaneously determine MMS, MSA and the eigenvector orientations with such a limited number of brain orientations in the magnetic field. That said, when DTI fiber tracking was first demonstrated (Mori et al., 1999), it took several hours on the animal scanner, and now this can be done in a few minutes on standard clinical platforms. We have no doubt the field of STI will progress rapidly in the coming years.

### Technical considerations

In addition to the noise in the MR phase measurements, limited head rotation range, and possible errors in fiber directions measured by DTI, the relatively low resolution in the DTI measurements may further increase the errors in the estimated diffusion tensor eigenvectors used for fitting the high resolution MMS and MSA. In this study, we were limited to 2.2 mm isotropic resolution for DTI data acquisition, which needed to be interpolated to 1 mm resolution in order to match the GRE phase data. In addition, the EPI distortion that exists in the DTI data may introduce certain coregistration errors especially around the frontal lobe as observed in this study. Better coregistration between the GRE phase data and the DTI data may be achieved in the future by employing LDDMM coregistration or other non-linear EPI distortion corrections.

As mentioned in the theory, assuming cylindrical symmetry, we can map the susceptibility tensor components by fitting MMS and MSA as in Eq. (8) and calculate  $\chi_{\parallel}$  and  $\chi_{\perp}$  to the fiber direction. On the other hand, we can also fit  $\chi_{\parallel}$  and  $\chi_{\perp}$  directly using Eq. (9) and subsequently calculate MMS and MSA. Our computer simulation (Fig. 6) shows that with SNR of 30, using four head orientations with head rotation angle of  $30^{\circ}$ , only small differences result from fitting MMS and MSA directly versus fitting  $\chi_{\parallel}$  and  $\chi_{\perp}$  directly. Most of the *in vivo* results (Fig. 8–10, Table 1) reported here were obtained by fitting MMS and MSA directly using Eq. (8). In addition, we also tested the alternative of fitting  $\chi_{\parallel}$  and  $\chi_{\perp}$  directly using Eq. (9) (Table 2). As compared to the values in Table 1, larger MSA values with an average of 0.022 ppm over the selected white matter regions were observed. This discrepancy may come from the different noise and error propagation properties of the two inverse mapping methods and need further theoretical analysis and simulation testing in the future.

While there are good reasons to expect susceptibility anisotropies in gray matter, we have restricted our reporting of MSA values to white matter regions. There are several reasons for this. First and foremost, we are using DTI information to derive the structural angles needed for calculating MSA. However the DTI eigenvectors in gray matter regions are known to be very unreliable due to the low FA and the arbitrary angles that will be found upon diffusion tensor diagonalization in such tissue. Second, the assumption of cylindrical symmetry may not apply to some of the gray matter structures. Third, with respect to the thin cortical ribbon, the resolution of DTI is about twice that of the current STI acquisition, leading to coregistration issues that affect the accuracy of the geometrical angles derived.

An interesting and unexpected phenomenon observed in this study is that even though the fitted MSA in most major white matter fibers was found to be positive, there were some fibers in which it was negative, for instance in the posterior limb of internal capsule (Fig. 8e, white arrow). A negative MSA suggests that the magnetic susceptibility along the fiber direction might be more diamagnetic, which seems unlikely in view of the consistent positive MSA results found for most of the white matter fibers (Fig. 10g). The most likely explanation therefore seems that incomplete removal of the background gradient when

determining the field shift in this region may lead to such a finding. Actually, the background gradient often flattens out in the middle of the brain, which generally is in the best shimmed area of the magnet, making it harder to fit out small variations in it.

The simulation study in Fig. 2 showed that the STI and isotropic susceptibility models differ by  $\pm 5 \times 10^{-3}$  ppm in the generated relative magnetic field shift for a susceptibility anisotropy value of 0.018 ppm, which corresponds to a resonance frequency shift of  $\pm 1.5$  Hz at 7 T and  $\pm 0.64$  Hz at 3 T. Therefore, the effects of anisotropy will become more apparent at higher field strengths because of the combined effects of increased susceptibility-based field shifts and higher SNR. However, current high field MR scanner coils generally have a more restricted space than scanners in the clinic (1.5 T and 3 T) and put more physical constraints on the range of possible head rotation angles. Better experimental strategies or numerical methods, such as the use of appropriate regularizations, may need to be developed in the future for *in vivo* mapping of the susceptibility anisotropy with better accuracy or for studying the fiber orientation based on the apparent susceptibility tensor in human brain, while using a small number of head orientations and small head rotation angles.

Finally, an alternative approach for susceptibility tensor analysis of anisotropic structures based on the cylindrical symmetry assumption would be the use of two polar angles (Bastiaan et al., 1987; Wharton and Bowtell, 2011) instead of three Cartesian coordinates to describe the orientation of the principal eigenvector; that is using:

$$\bar{v}_1^{sub} = [\sin\theta\cos\phi \quad \sin\theta\sin\phi \quad \cos\theta]^T$$

In this case, the number of unknowns in the STI inverse problem can be reduced from 6 to 4, namely MMS, MSA and the two polar angles. However, as shown in Eqs. (8) and (13), the mapping relationship between the four unknowns and the experimental observables would then be nonlinear, providing additional challenges in the data analysis.

$$\begin{aligned} \bar{T} &= \bar{I} - 3\bar{v}_1^{sub}(\bar{v}_1^{sub})^T \\ &= \begin{bmatrix} 1 - 3\sin^2\theta\cos^2\phi & -3\sin^2\theta\sin\phi\cos\phi & -3\sin\theta\cos\theta\cos\phi \\ & 1 - 3\sin^2\theta\sin^2\phi & -3\sin\theta\cos\theta\sin\phi \\ & & 1 - 3\cos^2\theta \end{bmatrix} \end{aligned} \quad (13)$$

## Conclusion

We showed that it is possible to measure MMS and MSA images by combining GRE phase data collected at four head orientations and fiber directions measured using DTI. We demonstrated the feasibility of this method in numerical simulations and subsequently applied it to whole brain phase data acquired *in vivo* on five healthy subjects at 7T. Good tissue contrast between gray and white matter was visible in the fitted MMS maps, and a positive mean MSA was consistently found in large white matter fiber bundles. These findings are in line with the expectation that the most paramagnetic susceptibility tensor component is parallel to the fiber direction.

## Acknowledgments

This project was supported by the National Center for Research Resources and the National Institute of Biomedical Imaging and Bioengineering of the National Institutes of Health through resource grant P41 EB015909. The authors would like to thank Mr. Joseph Gillen, Ms. Terri Brawner, Ms. Kathleen Kahl, Ms. Ivana Kusevic, and Dr. Raj Stewart for their assistance with data acquisition and Dr. Andreia Faria for her assistance with the determination of susceptibility values using white matter region from the DTI brain atlas. Dr. Peter van Zijl is a paid lecturer for

Philips Medical Systems and is the inventor of technology that is licensed to Philips. Dr. Craig Jones is paid in part through a grant to Kennedy Krieger Institute from Philips Medical Systems. This arrangement has been approved by The Johns Hopkins University in accordance with its Conflict of Interest policies.

## Appendix 1

Given a spatial distribution of a second-rank tensor field  $\bar{\chi}(\bar{r})$  using the Lorentz sphere correction (Chu et al., 1990), the magnetic flux density vector seen by any nucleus  $\bar{B}_{nuc}(\bar{r})$  is related to the macroscopic magnetic flux density  $\bar{B}_{mac}(\bar{r})$  as (Liu 2010; Salomir et al., 2003):

$$\bar{B}_{nuc} = \left( \bar{I} - \sigma \bar{I} - \frac{2}{3} \bar{\chi} \right) \cdot \bar{B}_{mac} \quad (\text{A.1})$$

where  $\sigma(\bar{r})$  is the chemical shift caused by the electrical screening effect and  $\bar{I}$  is the second rank identity tensor. The macroscopic magnetic flux density is proportional to the applied main magnetic field strength vector  $\bar{H}_0(\bar{r})$  and the demagnetization field  $\bar{h}_{obj}(\bar{r})$  caused by loading an object into the magnet as in:

$$\bar{B}_{mac} = \mu_0 \left( \bar{I} + \bar{\chi} \right) \cdot \left( \bar{H}_0 + \bar{h}_{obj} \right) \quad (\text{A.2})$$

where  $\mu_0$  is the vacuum permeability. In a modern MRI scanner and for most MR compatible material, the demagnetization field strength is much smaller than the applied main magnetic field strength, i.e.  $h_{obj} \ll H_0$  and the susceptibility tensor element  $|\chi_{ij}| \ll 1$ . Therefore, by combining Eqs. (A.1) and (A.2) and keeping only the first order terms, we can have:

$$\bar{B}_{nuc} = \mu_0 \left( \bar{I} - \sigma \bar{I} + \frac{1}{3} \bar{\chi} \right) \cdot \bar{H}_0 + \mu_0 \bar{h}_{obj} \quad (\text{A.3})$$

In the MR imaging object, the conduction current is zero (neglecting possible small eddy currents), therefore, the total macroscopic magnetic field strength vector can be considered irrotational:

$$\bar{\nabla} \times \left( \bar{H}_0 + \bar{h}_{obj} \right) = 0 \quad (\text{A.4})$$

This irrotational field can also be described by the gradient of a scalar magnetic potential as:

$$\left( \bar{H}_0 + \bar{h}_{obj} \right) = -\bar{\nabla} \left( \Phi_0 + \Phi_{obj} \right) \quad (\text{A.5})$$

In addition, according to Maxwell equations, we have the divergence of the macroscopic magnetic flux density to be zero:

$$\bar{\nabla} \cdot \bar{B}_{mac} = 0 \quad (\text{A.6})$$

When there is no object loading in the magnetic field, Eq. (A.6) can be simplified as:

$$\bar{\nabla} \cdot \bar{H}_0 = 0 \quad (\text{A.7})$$

Combining Eqs. (A.2), (A.6) and (A.7) and keeping only the first order terms, we can have:

$$\begin{aligned}\bar{\nabla} \cdot \bar{B}_{mac} &= \mu_0 \left[ \bar{\nabla} \cdot \bar{H}_0 + \bar{\nabla} \cdot \bar{h}_{obj} + \bar{\nabla} \cdot (\bar{\chi} \cdot \bar{H}_0) \right] \\ &= \mu_0 \left[ \bar{\nabla} \cdot \bar{h}_{obj} + (\bar{\nabla} \cdot \bar{\chi}) \cdot \bar{H}_0 \right] = 0\end{aligned}\quad (\text{A.8})$$

Note that we also assumed that the applied main magnetic field strength vector  $\bar{H}_0(\vec{r})$  is a constant vector over the imaging space, which is generally the case in practice. Using the magnetic potential  $\Phi_{obj}(\vec{r})$  as defined in Eq. (A.5), we can rewrite Eq. (A.8) as:

$$\bar{\nabla}^2 \Phi_{obj} = (\bar{\nabla} \cdot \bar{\chi}) \cdot \bar{H}_0 \quad (\text{A.9})$$

Taking the Fourier transform on both sides of (A.9) produces:

$$-k^2 \text{FT} \{ \Phi_{obj} \} = i\bar{k} \cdot \text{FT} \{ \bar{\chi} \} \cdot \bar{H}_0 \quad (\text{A.10})$$

where  $\bar{r}^2 = -1$  and  $k^2 = \|\bar{k}\|^2$ . From Eq. (A.10), we can now solve the magnetic potential of the demagnetizing field  $\Phi_{obj}(\vec{r})$  and further write out the demagnetization field vector as:

$$\Phi_{obj} = \text{FT}^{-1} \left\{ -\frac{i\bar{k} \cdot \text{FT} \{ \bar{\chi} \} \cdot \bar{H}_0}{k^2} \right\} \quad (\text{A.11})$$

$$\bar{h}_{obj} = -\text{FT}^{-1} \left\{ \bar{k} \frac{\text{FT} \{ \bar{\chi} \} \cdot \bar{H}_0}{k^2} \right\} \quad (\text{A.12})$$

Eq. (A.12) agrees with Eq. (7) in Ref (Liu 2010).

Combining Eqs. (A.3) and (A.12), the magnetic field shift  $\Delta \bar{B}_{nuc}$  referenced to  $\mu_0(1-\sigma)\bar{H}_0$  can be written as:

$$\Delta \bar{B}_{nuc} = \mu_0 H_0 \text{FT}^{-1} \left\{ \frac{1}{3} \text{FT} \{ \bar{\chi} \} \cdot \bar{H}_0 - \bar{k} \frac{\text{FT} \{ \bar{\chi} \} \cdot \bar{H}_0}{k^2} \right\} \quad (\text{A.13})$$

where  $\bar{H}_0 = H_0 \hat{H}_0$ . In MRI, the magnetic field shift that can be measured  $\Delta B$  is the projection of  $\Delta \bar{B}_{nuc}$  in the direction of the applied main magnetic field. Applying the dot product of  $\hat{H}_0$  on both sides of Eq.(A.13) and dividing both sides by  $\mu_0 H_0$  gives Eq. (1). Since  $\hat{H}_0$  is in the  $z$  direction in the MR lab frame of reference  $(x, y, z)$ , the measured field shift is generally denoted as  $\Delta B_z$ . As  $\Delta B_z$  depends on the main field strength, it is more convenient to use

the relative magnetic field shift  $\delta B_z = \frac{\Delta B_z}{B_0}$ , where  $B_0 = \mu_0 H_0$ .

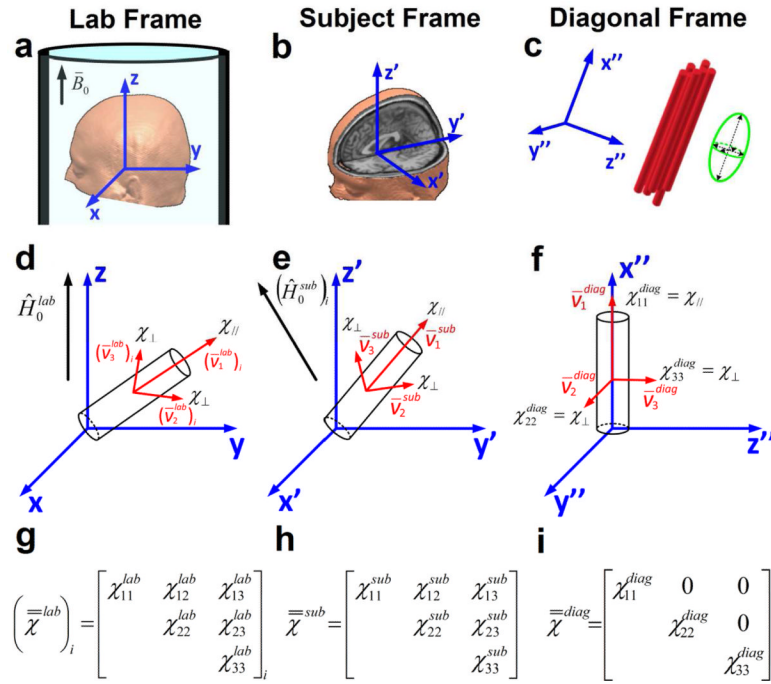
## Reference

- Albert MS, Huang W, Lee JH, Patlak CS, Springer CS Jr. Susceptibility changes following bolus injections. *Magn Reson Med*. 1993; 29(5):700–708. [PubMed: 8505909]
- Beg MF, Miller MI, Trounev A, Younes L. Computing large deformation metric mappings via geodesic flows of diffeomorphisms. *International Journal of Computer Vision*. 2005
- Basser PJ, Mattiello J, LeBihan D. MR diffusion tensor spectroscopy and imaging. *Biophysical Journal*. 1994; 66(1):259–267. [PubMed: 8130344]

- Bastiaan EW, MacLean C, van Zijl PCM, Bothner AA. High resolution NMR of liquids and gases: Effects of magnetic field induced molecular alignment. *Annual Reports on NMR Spectroscopy*. 1987; 9:35–77.
- Beaulieu C. The basis of anisotropic water diffusion in the nervous system - a technical review. *NMR in Biomedicine*. 2002; 15(7–8):435–455. [PubMed: 12489094]
- Chu SC, Xu Y, Balschi JA, Springer CS Jr. Bulk magnetic susceptibility shifts in NMR studies of compartmentalized samples: Use of paramagnetic reagents. *Magn Reson Med*. 1990; 13(2):239–262. [PubMed: 2156125]
- de Rochefort L, Brown R, Prince MR, Wang Y. Quantitative MR susceptibility mapping using piecewise constant regularized inversion of the magnetic field. *Magn Reson Med*. 2008; 60(4):1003–9. [PubMed: 18816834]
- de Rochefort L, Liu T, Kressler B, Liu J, Spincemaille P, Lebon V, Wu J, Wang Y. Quantitative susceptibility map reconstruction from MR phase data using bayesian regularization: Validation and application to brain imaging. *Magn Reson Med*. 2010; 63(1):194–206. [PubMed: 19953507]
- Denk C, Hernandez Torres E, MacKay A, Rauscher A. The influence of white matter fibre orientation on MR signal phase and decay. *NMR in Biomedicine*. 2011; 24(3):246–252. [PubMed: 21404336]
- Duyn JH, van Gelderen P, Li TQ, de Zwart JA, Koretsky AP, Fukunaga M. High-field MRI of brain cortical substructure based on signal phase. *Proc Natl Acad Sci U S A*. 2007; 104(28):11796–801. [PubMed: 17586684]
- Emsley, JW.; Lindon, JC. *NMR spectroscopy using liquid crystal solvents*. Pergamon Press; 1975.
- Fernandez-Seara MA, Techawiboonwong A, Detre JA, Wehrli FW. MR susceptometry for measuring global brain oxygen extraction. *Magn Reson Med*. 2006; 55(5):967–973. [PubMed: 16598726]
- Haacke EM, Xu Y, Cheng YC, Reichenbach JR. Susceptibility weighted imaging (SWI). *Magn Reson Med*. 2004; 52(3):612–618. [PubMed: 15334582]
- Haacke EM, Mittal S, Wu Z, Neelavalli J, Cheng YC. Susceptibility-weighted imaging: Technical aspects and clinical applications, part 1. *AJNR Am J Neuroradiol*. 2009; 30(1):19–30. [PubMed: 19039041]
- Haacke EM, Cheng NY, House MJ, Liu Q, Neelavalli J, Ogg RJ, Khan A, Ayaz M, Kirsch W, Obenaus A. Imaging iron stores in the brain using magnetic resonance imaging. *Magn Reson Imaging*. 2005; 23(1):1–25. [PubMed: 15733784]
- Hansen PC. The L-curve and its use in the numerical treatment of inverse problems. *Computational Inverse Problems in Electrocardiology*. 2000:119–124.
- He X, Yablonskiy DA. Biophysical mechanisms of phase contrast in gradient echo MRI. *Proc Natl Acad Sci U S A*. 2009; 106(32):13558–13563. [PubMed: 19628691]
- Hopkins JA, Wehrli FW. Magnetic susceptibility measurement of insoluble solids by NMR: Magnetic susceptibility of bone. *Magn Reson Med*. 1997; 37(4):494–500. [PubMed: 9094070]
- Jenkinson M, Bannister P, Brady M, Smith S. Improved optimization for the robust and accurate linear registration and motion correction of brain images. *NeuroImage*. 2002; 17(2):825–841. [PubMed: 12377157]
- Jiang H, van Zijl PC, Kim J, Pearlson GD, Mori S. DtiStudio: Resource program for diffusion tensor computation and fiber bundle tracking. *Computer Methods and Programs in Biomedicine*. 2006; 81(2):106–116. [PubMed: 16413083]
- Langham MC, Magland JF, Epstein CL, Floyd TF, Wehrli FW. Accuracy and precision of MR blood oximetry based on the long paramagnetic cylinder approximation of large vessels. *Magn Reson Med*. 2009; 62(2):333–340. [PubMed: 19526517]
- Lee J, Shmueli K, Fukunaga M, van Gelderen P, Merkle H, Silva AC, Duyn JH. Sensitivity of MRI resonance frequency to the orientation of brain tissue microstructure. *Proc Natl Acad Sci U S A*. 2010; 107(11):5130–5. [PubMed: 20202922]
- Li L. Magnetic susceptibility quantification for arbitrarily shaped objects in inhomogeneous fields. *Magn Reson Med*. 2001; 46(5):907–16. [PubMed: 11675642]
- Li W, Wu B, Liu C. Quantitative susceptibility mapping of human brain reflects spatial variation in tissue composition. *Neuroimage*. 2011a; 55(4):1645–56. [PubMed: 21224002]
- Li W, Wu B, Avram AV, Liu C. Magnetic susceptibility anisotropy of human brain in vivo and its molecular underpinnings. *NeuroImage*. 2011b doi: 10.1016/j.neuroimage.2011.10.038.

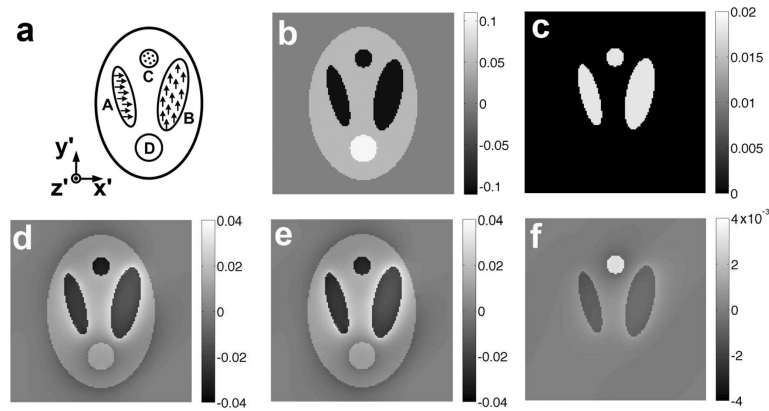
- Liu C. Susceptibility tensor imaging. *Magn Reson Med.* 2010; 63(6):1471–7. [PubMed: 20512849]
- Liu C, Li W, Johnson GA, Wu B. High-field (9.4T) MRI of brain dysmyelination by quantitative mapping of magnetic susceptibility. *Neuroimage.* 2011a; 56(3):930–8. [PubMed: 21320606]
- Liu C, Li W, Wu B, Jiang Y, Johnson GA. 3D fiber tractography with susceptibility tensor imaging. *NeuroImage.* 2011b doi:10.1016/j.neuroimage.2011.07.096.
- Liu T, Spincemaille P, de Rochefort L, Kressler B, Wang Y. Calculation of susceptibility through multiple orientation sampling (COSMOS): A method for conditioning the inverse problem from measured magnetic field map to susceptibility source image in MRI. *Magn Reson Med.* 2009; 61(1):196–204. [PubMed: 19097205]
- Liu T, Liu J, de Rochefort L, Spincemaille P, Khalidov I, Ledoux JR, Wang Y. Morphology enabled dipole inversion (MEDI) from a single-angle acquisition: Comparison with COSMOS in human brain imaging. *Magn Reson Med.* 2011; 66(3):777–783. [PubMed: 21465541]
- Marques JP, Bowtell R. Application of a fourier-based method for rapid calculation of field inhomogeneity due to spatial variation of magnetic susceptibility. *Concepts in Magnetic Resonance Part B-Magnetic Resonance Engineering.* 2005; 25B(1):65–78.
- Mittal S, Wu Z, Neelavalli J, Haacke EM. Susceptibility-weighted imaging: Technical aspects and clinical applications, part 2. *AJNR Am J Neuroradiol.* 2009; 30(2):232–52. [PubMed: 19131406]
- Mori S, Crain BJ, Chacko VP, van Zijl PC. Three-dimensional tracking of axonal projections in the brain by magnetic resonance imaging. *Annals of Neurology.* 1999; 45(2):265–269. [PubMed: 9989633]
- Mori S, Oishi K, Jiang H, Jiang L, Li X, Akhter K, Hua K, Faria AV, Mahmood A, Woods R, et al. Stereotaxic white matter atlas based on diffusion tensor imaging in an ICBM template. *NeuroImage.* 2008; 40(2):570–582. [PubMed: 18255316]
- Oishi K, Faria A, Jiang H, Li X, Akhter K, Zhang J, Hsu JT, Miller MI, van Zijl PC, Albert M, et al. Atlas-based whole brain white matter analysis using large deformation diffeomorphic metric mapping: Application to normal elderly and alzheimer's disease participants. *NeuroImage.* 2009; 46(2):486–499. [PubMed: 19385016]
- Paige CC, Saunders MA. LSQR: An algorithm for sparse linear equations and sparse least squares. *ACM Transactions on Mathematical Software.* 1982; 8(1):43–71.
- Salomir R, De Senneville BD, Moonen CTW. A fast calculation method for magnetic field inhomogeneity due to an arbitrary distribution of bulk susceptibility. *Concepts in Magnetic Resonance Part B-Magnetic Resonance Engineering.* 2003; 19B(1):26–34.
- Schenck JF. Physical interactions of static magnetic fields with living tissues. *Progress in Biophysics and Molecular Biology.* 2005; 87(2–3):185–204. [PubMed: 15556658]
- Schweser F, Deistung A, Lehr BW, Reichenbach JR. Quantitative imaging of intrinsic magnetic tissue properties using MRI signal phase: An approach to in vivo brain iron metabolism? *Neuroimage.* 2011; 54(4):2789–807. [PubMed: 21040794]
- Shmueli K, de Zwart JA, van Gelderen P, Li TQ, Dodd SJ, Duyn JH. Magnetic susceptibility mapping of brain tissue in vivo using MRI phase data. *Magn Reson Med.* 2009; 62(6):1510–22. [PubMed: 19859937]
- Smith SM. Fast robust automated brain extraction. *Human Brain Mapping.* 2002; 17(3):143–155. [PubMed: 12391568]
- Smith SM, Jenkinson M, Woolrich MW, Beckmann CF, Behrens TE, Johansen-Berg H, Bannister PR, De Luca M, Drobnjak I, Flitney DE, et al. Advances in functional and structural MR image analysis and implementation as FSL. *NeuroImage.* 2004; 23(Suppl 1):S208–19. [PubMed: 15501092]
- van Zijl PCM, Ruessink BH, Bulthuis J, MacLean C. NMR of partially aligned liquids: Magnetic susceptibility anisotropies and dielectric properties. *Acc. Chem. Res.* 1984; 17:172–180.
- Wharton S, Bowtell R. Whole-brain susceptibility mapping at high field: A comparison of multiple- and single-orientation methods. *Neuroimage.* 2010; 53(2):515–25. [PubMed: 20615474]
- Wharton S, Bowtell R. A simplified approach for anisotropic susceptibility map calculation. *Proceedings of International Society for Magnetic Resonance in Medicine.* 2011; 19:4515.
- Wharton S, Schafer A, Bowtell R. Susceptibility mapping in the human brain using threshold-based k-space division. *Magn Reson Med.* 2010; 63(5):1292–304. [PubMed: 20432300]

- Wu B, Li W, Guidon A, Liu C. Whole brain susceptibility mapping using compressed sensing. *Magn Reson Med*. 2011; 67(1):137–47. [PubMed: 21671269]
- Zecca L, Youdim MB, Riederer P, Connor JR, Crichton RR. Iron, brain ageing and neurodegenerative disorders. *Nat Rev Neurosci*. 2004; 5(11):863–73. [PubMed: 15496864]

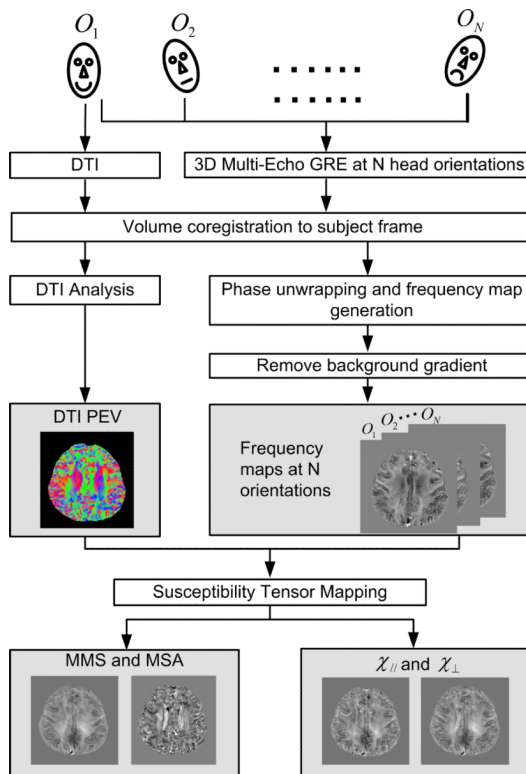
**FIG. 1.**

Definition of reference frames and tensor components. (a) The laboratory (lab) frame of reference ( $x, y, z$ ), (b) the subject (sub) frame of reference ( $x', y', z'$ ) and (c) the diagonal (diag) frame of reference ( $x'', y'', z''$ ). The lab frame is defined with respect to the direction of the magnetic field flux density vector  $\bar{B}_0$ . The subject frame is defined with respect to the midsagittal plane and the plane perpendicular through it including the anterior commissure – posterior commissure (AC-PC) line. The diagonal frame of reference is defined by the principal axes of the susceptibility tensor in each image voxel and is assumed to be aligned with the direction of the white matter fibers (most paramagnetic susceptibility and largest diffusion constant) in that voxel. The spatial relationship between the three reference frames and the cylindrically symmetric magnetic susceptibility tensor in white matter fibers is illustrated in (d), (e) and (f).  $\hat{H}_0$  denotes the unit vector in the direction of the applied magnetic field;  $\bar{v}_1, \bar{v}_2, \bar{v}_3$  are the three eigenvectors of the susceptibility tensor, which, in white matter fibers, are assumed to be the same as the corresponding eigenvectors of the diffusion tensor;  $\bar{v}_1$  is the principal eigenvector describing the fiber direction.  $\chi_{\parallel}$  and  $\chi_{\perp}$  are the eigenvalues of the magnetic susceptibility tensor parallel and perpendicular to the fiber direction, respectively. The expressions for the magnetic susceptibility tensor of a white matter voxel in the lab frame, subject frame and diagonal frame are shown in (g), (h) and (i),

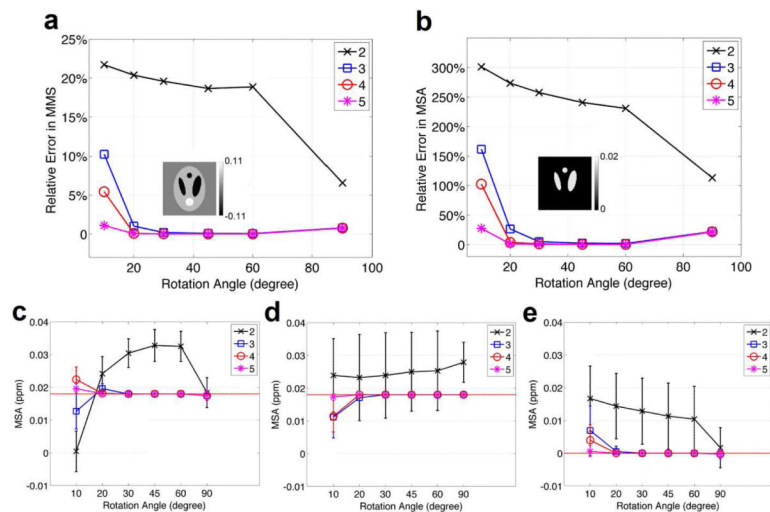
respectively. The selected frame of reference is in superscript.  $(\bar{\chi}^{lab})_i$  and  $(\hat{H}_0^{sub})_i$  denote the susceptibility tensor and the main magnetic field strength direction at the  $i$ th head orientation in the lab frame of reference and subject frame of reference, respectively. Since all tensor variables are assumed symmetric, only the upper part is written out explicitly.

**FIG. 2.**

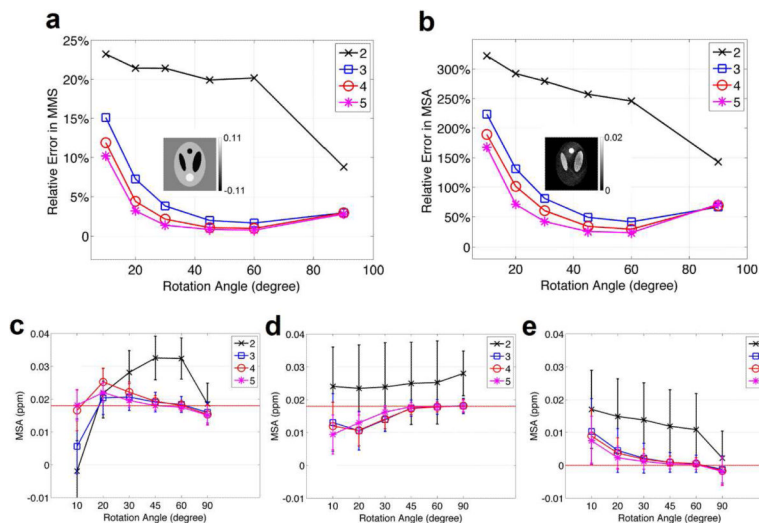
(a) Diagram of the central slice of the numerical head phantom used in our simulation study. Three ellipsoid objects (A, B and C) with anisotropic cylindrically symmetric susceptibility tensor distributions are included to simulate white matter regions with fibers oriented in different directions (indicated by small arrows); other parts of the phantom (D and background) have isotropic susceptibility values. The definition of the subject frame ( $x'$ ,  $y'$ ,  $z'$ ) is with main axis ( $z'$ ) perpendicular to the slice plane shown in this diagram. (b) Target mean magnetic susceptibility (MMS) image. (c) Target magnetic susceptibility anisotropy (MSA) image. In the anisotropic objects (A, B and C),  $MMS = -0.100$  ppm and  $MSA = 0.018$  ppm. In the isotropic object (D),  $MMS = 0.100$  ppm and in the remaining isotropic area  $MMS = 0.05$  ppm. (d–e) Simulated relative field change maps ( $\delta B_z$ ) at the normal head position using the susceptibility tensor model (d) and an isotropic susceptibility model (e). (f) Difference between the simulated relative field change maps in (d) and (e), showing that the field shift map generated from the isotropic model deviates from that generated from the exact tensor model for structures with anisotropic susceptibility and that the sign of the deviation depends on the orientation of the microstructure. All units are in ppm.



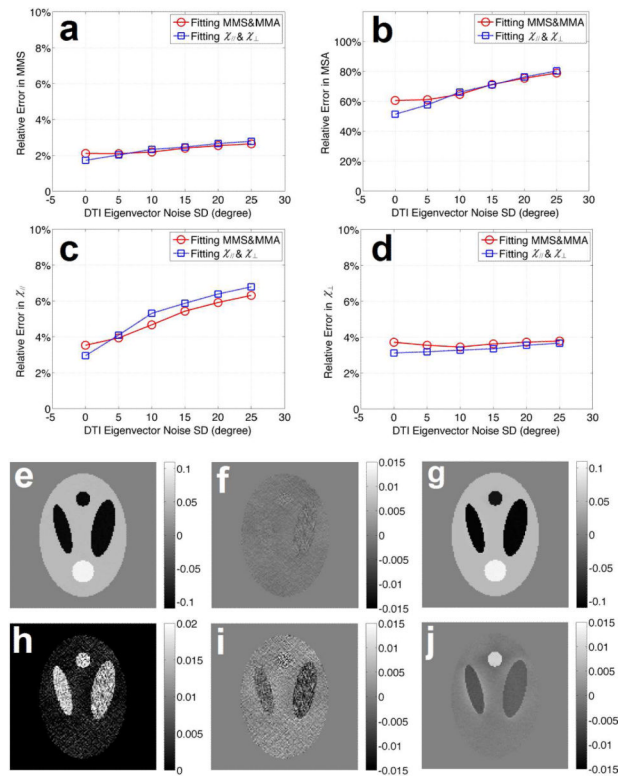
**FIG. 3.** A flow chart showing the steps of the procedure for mapping MMS and MSA using both GRE phase data and fiber direction information (the principal eigenvector (PEV) of the diffusion tensor) obtained from DTI.



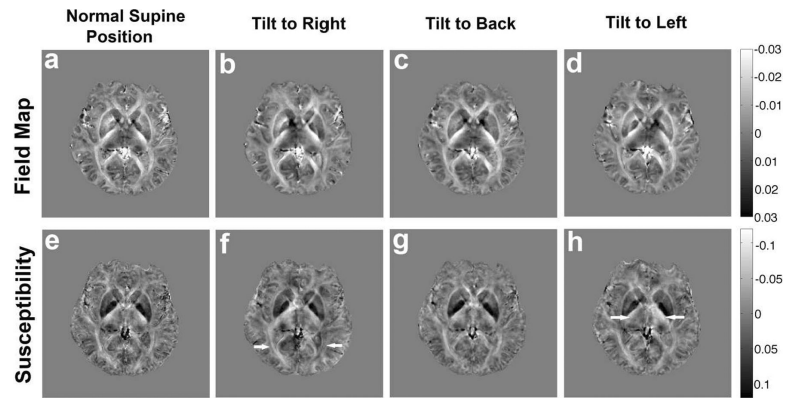
**FIG. 4.** Relative errors in the reconstructed MMS (a) and MSA (b) maps for the head phantom under noise free conditions as a function of head rotation angle and number of head orientations. The numbers 2–5 in each legend represent the number of head orientations used. The embedded images are central slice images of the MMS (a) and MSA (b) maps reconstructed using four head orientations with rotation angle of  $30^\circ$ . Grayscale units are in ppm. (c–e) Mean MSA value ( $\pm$  S.D.) as a function of rotation angle and number of head rotations for anisotropic region C that has principal eigenvectors parallel to  $z'$  (c), over anisotropic regions A and B that have principal eigenvectors perpendicular to  $z'$  (d) and over all isotropic regions (e). The target MSA values are marked by the red dotted lines.



**FIG. 5.** Relative errors in the reconstructed MMS (a) and MSA (b) maps as a function of head rotation angle and number of head orientations using simulated magnetic field shift data with SNR of 30 and noise free DTI eigenvectors. The numbers 2–5 in each legend represent the number of head orientations used. The embedded images are central slice images of the MMS (a) and MSA (b) maps reconstructed using four head orientations with rotation angle of 30°. Grayscale units are in ppm. (c–e) Mean MSA values ( $\pm$  S.D.) as a function of rotation angle and number of head rotations for anisotropic region C that has principal eigenvectors parallel to  $z'$  (c), over anisotropic regions A and B that have principal eigenvectors perpendicular to  $z'$  (d) and over all isotropic regions (e). The target MSA values are marked by the red dotted lines.

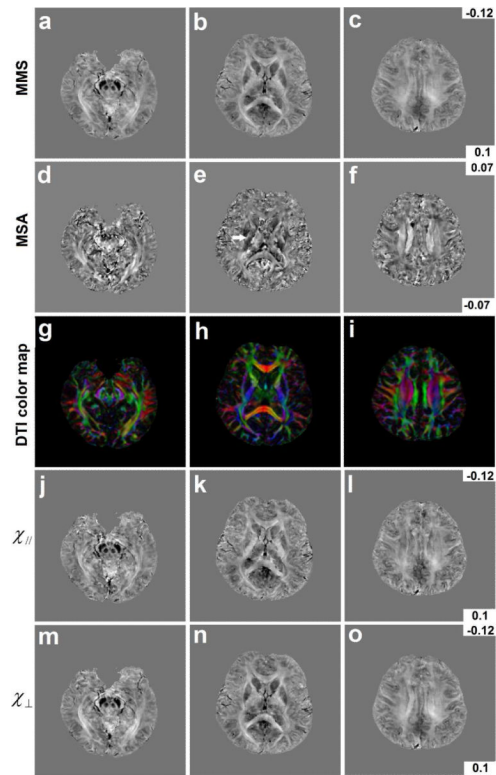
**FIG. 6.**

Relative errors in the reconstructed MMS (a), MSA (b),  $\chi_{\parallel}$ (c) and  $\chi_{\perp}$  (d) as a function of added Gaussian angular noise in the DTI eigenvectors using simulated magnetic field shift data with SNR of 30 at four head orientations with rotation angle of  $30^{\circ}$ . Results obtained from directly fitting MMS and MSA using Eq. 8 (red line) are compared with those obtained from directly fitting  $\chi_{\parallel}$  and  $\chi_{\perp}$  using Eq. 9 (blue line). (e) and (h) are the central axial slice of the reconstructed MMS (e) and MSA (h) maps for a standard deviation in angular noise of  $10^{\circ}$ . (f and i) Images of the error in the reconstructed MMS and MSA maps corresponding to (e) and (h). (g) Reconstructed isotropic susceptibility map obtained using the multiple-orientation QSM method. (j) Difference image between the reconstructed isotropic susceptibility map and the target MMS map, showing that the isotropic model deviates from the exact tensor model for anisotropic structures and that the sign of the deviation depends on the orientation of the microstructure. All grayscale units are in ppm.



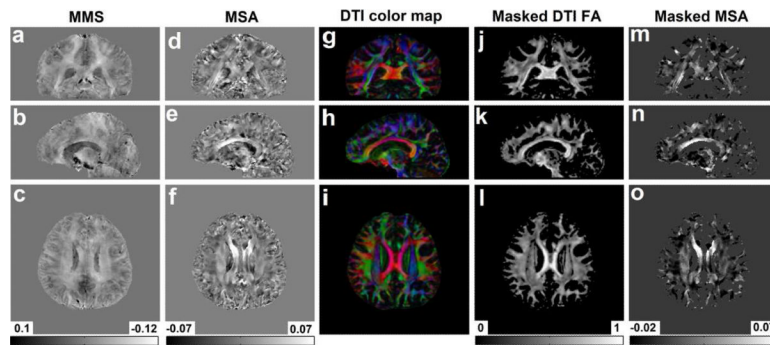
**FIG. 7.**

(a – d) Example axial slice of the relative field change map ( $\delta B_z^{sub}$ ) obtained in a single subject at four different head orientations. (a) Normal supine position; (b) tilt to right shoulder ( $19^\circ$  around AP axis); (c) tilt to back ( $12^\circ$  around RL axis); (d) tilt to left shoulder ( $8^\circ$  around AP axis). (e – h) Reconstructed apparent susceptibility maps at the same four head orientations obtained assuming isotropic susceptibility and using the LSQR method and phase data obtained at each single head orientation. Lower field and lower magnetic susceptibility are indicated by higher image intensity to better visualize the white matter, which generally exhibits negative magnetic susceptibility relative to CSF. White arrows mark white matter regions showing orientation dependence in the apparent susceptibility maps as evident in left-right asymmetry. All units are in ppm.

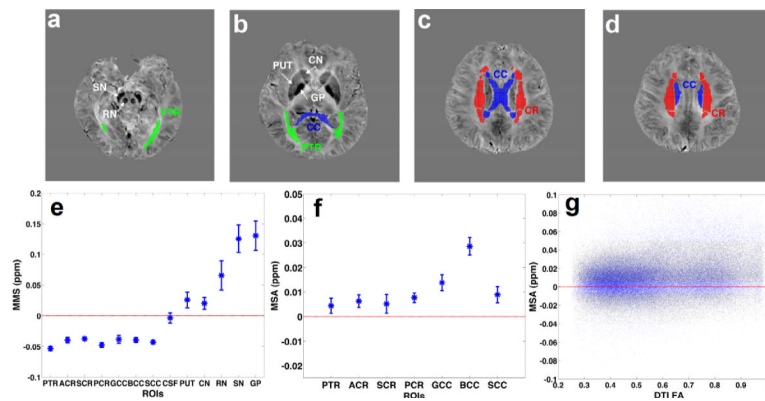


**FIG. 8.**

Axial slices of the MMS (a – c) and MSA map (d – f) of a single subject. The white arrow masks the posterior limb of the internal capsule. (g – i) Corresponding DTI color maps. Corresponding ( $\chi_{\parallel}$ ) (j – l) and ( $\chi_{\perp}$ ) (m – o) maps. All gray scale units are in ppm. In MMS,  $\chi_{\parallel}$  and  $\chi_{\perp}$  maps, lower magnetic susceptibility is indicated by higher intensity to better visualize the white matter, which has negative magnetic susceptibility. In MSA maps a normal gray scale is used for the same reason.



**FIG. 9.** Coronal, sagittal and axial slices of the reconstructed MMS (a–c), MSA (d–f), DTI color (g–i), white matter masked DTI FA (j–l) and white matter masked MSA (m–o) maps to illustrate the image quality in three dimensions. The white matter mask used in (j–o) was obtained by thresholding  $FA > 0.25$ . The gray scales for MMS and MSA maps are in ppm; for FA the typical normalized scale is used. It can be seen that the white matter magnetic susceptibility anisotropy is positive for most white matter areas, but that the SNR is not yet as good as for FA.

**FIG. 10.**

(a–d) Details of region selection for MMS and MSA data analysis as visualized by color superposition on the mean magnetic susceptibility (MMS) map of a single subject. Some deep gray matter structures are also marked by arrows. (e) MMS and (f) MSA values for all selected white matter averaged over all five subjects (mean  $\pm$  S.D.). Some selected gray matter regions are also included in (e). (g) A scatter plot of the MSA values in all selected white matter voxels of all five subjects as a function of the corresponding FA values. No correlation is apparent. Abbreviations: SN: substantia nigra; RN: red nucleus; GP: globus pallidus; PUT: putamen; CN: caudate nucleus; PTR: posterior thalamic radiations (including optic radiations); CR: corona radiata; ACR: anterior corona radiata; SCR: superior corona radiata; PCR: posterior corona radiata; CC: corpus callosum; GCC: genu of corpus callosum; BCC: body of corpus callosum; SCC: splenium of corpus callosum.

**Table 1**

Fitted mean magnetic susceptibility (MMS) and magnetic susceptibility anisotropy (MSA) using Eq. (8) together with the calculated magnetic susceptibility tensor components parallel ( $\chi_{\parallel}$ ) and perpendicular ( $\chi_{\perp}$ ) to the fiber direction in selected central white matter regions (n=5).

ROIs	MMS (ppm)		MSA (ppm)		$\chi_{\parallel}$ (ppm)		$\chi_{\perp}$ (ppm)	
	Mean	SD	Mean	SD	Mean	SD	Mean	SD
<b>PTR</b>	-0.053	0.0033	0.0044	0.0031	-0.050	0.0048	-0.055	0.0028
<b>ACR</b>	-0.039	0.0045	0.0063	0.0025	-0.035	0.0036	-0.041	0.0051
<b>SCR</b>	-0.037	0.0023	0.0052	0.0038	-0.034	0.0020	-0.039	0.0033
<b>PCR</b>	-0.047	0.0039	0.0077	0.0019	-0.042	0.0044	-0.050	0.0038
<b>GCC</b>	-0.038	0.0062	0.014	0.0032	-0.029	0.0046	-0.043	0.0071
<b>BCC</b>	-0.039	0.0037	0.029	0.0037	-0.020	0.0033	-0.049	0.0045
<b>SCC</b>	-0.043	0.0026	0.0089	0.0033	-0.037	0.0023	-0.046	0.0033
<b>All</b>	-0.042	0.0023	0.010	0.0022	-0.035	0.0016	-0.045	0.0029

**Table 2**

Fitted magnetic susceptibility tensor components parallel ( $\chi_{\parallel}$ ) and perpendicular ( $\chi_{\perp}$ ) to the fiber direction using Eq. (9) together with the calculated MMS and MSA in selected central white matter regions (n=5).

ROIs	MMS (ppm)		MSA (ppm)		$\chi_{\parallel}$ (ppm)		$\chi_{\perp}$ (ppm)	
	Mean	SD	Mean	SD	Mean	SD	Mean	SD
<b>PTR</b>	-0.047	0.0027	0.022	0.0046	-0.033	0.0047	-0.054	0.0027
<b>ACR</b>	-0.038	0.0039	0.017	0.0055	-0.026	0.0017	-0.044	0.0056
<b>SCR</b>	-0.036	0.0021	0.0082	0.0054	-0.031	0.0020	-0.039	0.0038
<b>PCR</b>	-0.043	0.0025	0.017	0.0040	-0.032	0.0050	-0.049	0.0015
<b>GCC</b>	-0.037	0.0052	0.029	0.0069	-0.018	0.0019	-0.047	0.0073
<b>BCC</b>	-0.040	0.0029	0.045	0.0065	-0.010	0.0022	-0.055	0.0050
<b>SCC</b>	-0.040	0.0022	0.023	0.0071	-0.025	0.0044	-0.048	0.0038
<b>All</b>	-0.040	0.0019	0.022	0.0041	-0.025	0.0012	-0.047	0.0032